공학박사학위논문

Generation of charged nanoparticles and their effects on Ti film deposition during RF magnetron sputtering

RF 마그네트론 스퍼터링 내에서 하전된
나노입자의 생성과 이들이 박막 증착 거동에
미치는 영향

2020년 8월

서울대학교 대학원

재료공학부

권 지 혜

Generation of charged nanoparticles and their effects on Ti film deposition during RF magnetron sputtering

지도교수 황 농 문

이 논문을 공학박사 학위논문으로 제출함

2020 년 8 월

서울대학교 대학원

재료공학부

권 지 혜

권지혜의 공학박사 학위논문을 인준함

2020 년 8 월

위 원 장   박 은 수   (인)

부위원장   황 농 문   (인)

위　　원   장 호 원   (인)

위　　원   유 병 덕   (인)

위　　원   박 진 우   (인)

Abstract

Generation of charged nanoparticles and their effects on Ti film deposition during RF magnetron sputtering

Ji Hye Kwon

Department of Materials Science and Engineering

The Graduate School

Seoul National University

Generation of charged nanoparticles (NPs) during RF sputtering using titanium (Ti) target was confirmed and their influence on film quality was investigated. Charged Ti NPs were captured on amorphous carbon membranes with the electric bias of -70, 0, $+5$, $+15$ and $+30$V and examined by transmission electron microscopy (TEM). The number density of the Ti NPs decreased with increasing positive bias, which showed that some of Ti NPs were positively charged and

i

repelled by the positively biased TEM membrane. Ti films were deposited on silicon (Si) substrates with the bias of −70, 0 and +30V and analyzed by TEM, field−emission scanning electron microscopy (FESEM) and X−ray reflectivity (XRR). The film deposited at −70V had the highest thickness, crystallinity and density, whereas the film deposited at +30V had the lowest quality. This was attributed to the attraction of positively charged Ti NPs to the substrate at −70V and to the landing of only small−sized neutral Ti NPs on the substrate at +30V. These results indicate that the control of charged NPs is necessary to obtain high quality thin film at room temperature.

Also, the possibility of preparing highly (002) oriented Ti films on the Si (100) substrate was studied using RF sputtering. The deposition behavior was compared between floating and grounded substrates at room temperature. Highly (002) oriented Ti films could be successfully prepared on the floating Si (100) substrate, which was revealed by X−ray diffraction (XRD) and high resolution TEM. To understand the different deposition behavior between floating and grounded substrates, the incident energy of ions during RF sputtering was estimated from the substrate temperature measured by the K−type thermocouple. The incident energy on the floating substrate was lower by 20% than that on the grounded substrate. It was

suggested that the lower incident energy on the floating substrate would be responsible for the deposition of highly (002) oriented Ti films at room temperature.

Meanwhile, it is also necessary to conduct in-situ plasma diagnostics during the process for investigating the consistent plasma condition and further information of the plasma. When the same plasma condition is remained, the consistent and reliable experiment results can be obtained. However, the plasma condition could be sensitive to small changes and affect the entire process and results. Also, various plasma diagnostics technique can broadly provide the information of the plasma condition such as electron and ion temperature, plasma density. Using in-situ plasma diagnostics, we characterized neutral and positively charged species of Ar and Ti in the plasma. Existence and proportion of Ti and Ar species at different process pressure were investigated by optical emission spectroscopy (OES). Also, the energy distribution of the positively charged species were estimated by ion energy analyzer. Using this result, the energy distribution of positively charged Ti NPs were confirmed experimentally. Therefore, in-situ plasma diagnostics is recommended to understand the plasma process and results correctly.

List of Figures

List of Tables

Contents

Chapter 1. Introduction

Chapter 2.

Generation of charged Ti nanoparticles and their deposition behavior with substrate bias during RF magnetron sputtering

Chapter 3.

Preparation of highly (002) oriented Ti films on a floating Si (100) substrate by RF magnetron sputtering

Chapter 4.

In-situ plasma diagnostics for investigating charged species during Ti RF magnetron sputtering

Chapter 1. Introduction

1.1. Non-classical crystallization

The theory of classical crystal growth was established based on the concept that the building block of crystals should be individual ions, atoms, or molecules. According to text books related to thin film growth by chemical vapor deposition (CVD), atoms or molecules are formed on the growing surface or in the gas phase as a result of chemical reactions of reactant gases. Those atoms or molecules are then adsorbed on a terrace, diffused to a ledge and become incorporated in the crystal lattice at the kink, which is called the terrace, ledge, and kink (TLK) model [1, 2].This mechanism is called 'classical crystal growth mechanism'. Normally, a ledge of monoatomic height is regarded as a kink because the ledge is disordered or rough, consisting of lots of kinks. An atom on the terrace, which is called an adatom, has excess broken bonds but an atom at the kink has no excess broken bond. For this reason, a reversible transfer of atoms occurs only at kinks during condensation or evaporation. In other words, the interaction of

atoms or molecules with the terrace is repulsive; but, their interaction with the kink is attractive.

However, there have been some experimental results, which cannot be properly explained by this classical mechanism. Rather such experimental results strongly imply that crystals should grow by the building blocks of nanoparticles (NPs), whose concept of crystal growth is called 'non-classical crystallization' [3-7]. This new growth mechanism has difficult to accept generally for some reasons at first. Because charged NPs are invisible due to their small size less than the wavelength range of visible light. In addition, it is difficult to be convinced that dense films and nanostructures are made by the building block of charged NPs. However, recently, non-classical crystallization was confirmed by in-situ transmission electron microscope (TEM) observations and it has now become so established that a few related books have been published and introduced in tutorial and technical sessions of international conferences. With the establishment of non-classical crystallization, many crystals that were believed to grow by atomic, molecular, or ionic entities turn out to grow actually by NPs. Non-classical crystallization can be applied to crystal growth not only in solution like a colloidal process but also in the gas phase synthesis of thin films and nanostructures

by CVD and physical vapor deposition (PVD). Hwang et al. [8-12] extensively studied non-classical crystallization in the CVD process, publishing text books and more than 80 SCI papers. They suggested that the electric charge having the NPs played an important role in the growth of thin films and nanostructures and could make NPs to be the building block of the crystal growth. Therefore, this new growth mechanism in the gas phase synthesis is called 'theory of charged nanoparticles (TCN)'. According to this theory, charged NPs, which are spontaneously generated in the gas phase in most CVD processes, contribute to the growth of thin films and nanostructures. If NPs are neutral, they are coagulated by random Brownian motion and produce a porous structure. On the other hand, if NPs are charged, they deposit as dense films. This results from that charged NPs undergo self-assembly. Since charge having NPs weakens the bond strength, it makes NPs to be liquid-like and epitaxial recrystallization to be possible. For the more details of classical and non-classical crystallization, crystalline pathways between classical and non-classical crystallization are compared in Figure 1. The building blocks of classical crystallization are atoms, ions, or molecules, which form NPs [13]. As described in the classical nucleation theory, these NPs may grow or shrink by the relative

magnitude of surface and bulk energies. If NPs reach the size of the critical nucleus, they can continue to grow into macro crystals by the attachment of an individual atom or molecule.

In diamond deposition process in CVD, under the same deposition condition where diamond films grow on a silicon substrate, very porous graphitic soot particles grow on an iron substrate as shown in Figure 2 [7, 14]. These results indicate that the deposition mechanisms of diamond and soot should be related to each another. From a preliminary study charged diamond nuclei deposit as a diamond film and soot respectively on silicon and iron substrates. Also, this deposition behavior is correlated with the charge transfer rate of the substrate which diamond is generated on the substrate having a low charge transfer rate whereas soot is generated on the substrate having a high charge transfer rate. According to Hwang et al. [9], when negatively charged diamond nuclei approach the silicon substrate having a low charge transfer rate, they remain a diamond phase and undergo self-assembly like a colloidal of nanometer unit, resulting in the diamond film as shown in Figure 2(a). However, when negatively charged diamond nuclei approach the iron substrate having a high charge transfer rate, they lose charge to the iron substrate just before landing and get changed to graphite. And the neutral graphite NPs undergo

random Brownian coagulations and generate porous soot on the iron substrate as shown in Figure 2(b). In this understanding, charge is responsible for the stability of diamond. That means if carbon NPs are charged, they maintain a diamond structure, but if they are not charged, they have a graphite structure. To confirm the effect of charge on the stability of diamond, Hwang et al. [9] compared the deposition behavior between floating and grounded iron substrates. On the grounded iron substrate, soot particles continued to grow. However, on the floating iron substrate, soot particles initially were formed and then diamond crystals finally were grown.

Moreover, the generation of CNPs in the gas phase was experimentally confirmed using a differential mobility analyzer (DMA) in many CVD systems as shown in Figure 3 [15-17]. Hwang et al. [9, 10] suggested that these CNPs are the building blocks of thin films and nanostructures in most CVD processes. To show CNPs to be building blocks of thin films or nanostructures in a silicon CVD process, Youn et al. [18] confirmed the generation of CNPs in the gas phase by differential mobility analyzer (DMA) as shown in Figure 3 and compared the deposition behavior between floating and grounded silicon substrates in HWCVD system. Charge build-up would be maximized on the floating substrate and minimized

on the grounded substrate. The result is shown in Figure 4. Figure 4(a) and (b) shows respectively low- and high-magnification FESEM images of the surface microstructure deposited on the floating substrate for 2 hours. The substrate temperature is 900° C and the gas flow rates are 5 sccm SiH$_4$:He (1:9), 50 sccm H$_2$, and 500 sccm N$_2$. Figure 4(c) and (d) shows respectively low- and high-magnification FESEM images of the surface microstructure of the grounded substrate deposited under the same as Figure 4(a) and (b). Silicon nanowires of diameter in 10 ~ 30 nm grew on the floating substrate as shown in Figure 4(a) and (b), whereas silicon NPs were deposited on the grounded substrate as shown in Figure 4(c) and (d). In Figure 4(b), without catalytic metals or seeds of silicon oxide, silicon nanowires were grown on the substrate. Neither vapor-liquid-solid (VLS) [19] nor oxide-assisted growth (OAG) [20] mechanism can explain this deposition behavior. Therefore, charge build-up would be the only difference between Figure 4(b) and (d) because floating and grounded of the substrate are the only differences in the process between Figure 4(b) and (d). With respect to this difference, the growth of silicon nanowires would be attributed to the charge build-up. In other words, the electrostatic interaction between the charged NPs and the substrate affects

the growth of the silicon nanowires. As increasing the N_2 flow rate from 500 to 1000 sccm, no nanowires but films were grown as shown in Figure 5. Figure 5(a) and (b) shows respectively top view and cross−section view FESEM images of the films deposited on floating silicon substrates. Figure 5(c) and (d) shows those deposited on a grounded substrate. Different microstructures were evolved between the floating and grounded substrates. This result indicate that in Figure 5(a) and (b), the dense film with ~220 nm thickness was deposited on a floating substrate by the electrostatic interaction between the charged NPs and the growing surface, whereas in Figure 5(c) and (d), porous with ~190 nm thickness was deposited on a grounded substrate due to negligible electrostatic interaction on the growing surface. Therefore, the amount of aggregated species on the floating substrate in Figure 5(b) is much larger than that on the grounded substrate in Figure 5(d). This study also indicates that the deposition behavior of charged silicon NPs is clearly different between floating and grounded substrates because of the difference in the charge build−up on surface between floating and grounded substrates. These results indicate that charge plays an important role in producing smooth nanowires and dense films.

According to Hwang et al. [11, 12], the supersaturation that

triggers the gas-phase nucleation turns out to be so low that the film growth rate without gas-phase nucleation is quite low. Thus the processing conditions with a low growth rate would not be considered as a candidate in the thin film industry. In other words, the gas-phase nucleation occurs generally and is inevitable under the process conditions of commercially available thin films in most CVD and some PVD systems. It was believed that the gas-phase nucleation would be detrimental to the thin film growth. Gas phase-generated NPs may result in fatal defects and failure of devices, due to small feature sizes [21]. On the other hand, Hwang et al. [12] suggested that the deposition behavior of gas phase-generated nanoparticles differs dramatically according to whether they are electrically charged or not. Neutral NPs generate a porous skeletal structure and degrade the film qualities. However, charged NPs, which are liquid-like, deposit epitaxially dense films without voids. The film microstructures deposited by liquid-like charged NPs would be similar with those deposited by individual atoms or molecules, but growth rate would be different between the films deposited by charged NPs and those by individual atoms. Therefore, to obtain a high quality film with high growth rate, it would be necessary to use the generation of charged NPs in the gas phase. In accordance with this new

understanding, Yoshida et al. [22] could grow high T_c superconducting ($YBa_2Cu_3O_{7-x}$) films epitaxially at a rate as high as 16 nm/s by supplying $YBa_2Cu_3O_{7-x}$ particles using the plasma flash evaporation method. Cabarrocas et al [23, 24] also utilize the incorporation of gas phase−nucleated nanoparticles in the plasma−enhanced CVD (PECVD) process. During the deposition of silicon by PECVD, Cabarrocas et al deposited polymorphous films, where gas phase−generated crystalline silicon nanoparticles are incorporated into the films. Polymorphous films have better stability and electrical properties than amorphous films.

Figure 6 shows the TEM images of the nanocrystals which are connected by a neck at the initial stage of coalescence. Neck growth occurs simultaneously with decreasing length (l) and thickness (t), which means that the atoms migrate to the neck region by surface diffusion [25]. After coalescence, the nanocrystal structure gradually reorganizes, evolving truncated surfaces. Figure 6 shows the detailed process how crystalline growth occurs by the building blocks of NPs. Yuk et al. [26] mentioned supporting information that all images were analyzed under ambient conditions at 23° C. It imply that such enhanced kinetics of liquid−like coalescence at a low temperature would result from charged nanocrystals because charging is

9

unavoidable during TEM observation although the authors did not mention the role of charge.

Considering that charged NPs are liquid-like, it is expected that the bond strength should be weakened by the presence of charge. To confirm this possibility, we made an extensive literature survey. Clare et al. [27] studied the effect of charge on the bond strength in hydrogenated amorphous silicon. The effect of a single negative or positive charge on the strength of Si-Si and Si-H bonds in the molecules SiH_4 and Si_2H_2 was calculated by ab initio calculations. To determine the difference in the energy to break a single Si-H bond in SiH_4, SiH_4^+ and SiH_4^- calculations were done on six species: SiH_3, SiH_4, SiH_3^-, SiH_4^-, SiH_3^+, and SiH_4^+ and the required energies were determined by comparing the bond strength of each species. Similar calculations were done with the species Si_2H_6, Si_2H_5, $Si_2H_6^-$, $Si_2H_5^-$, $Si_2H_6^+$, and $Si_2H_5^+$ to observe the effect of a lower charge/size ratio and to examine the effect of charge on the Si-Si bond energy. The results of ab initio calculations are shown in Table 1. When the atoms are embedded in a lattice, they will not be free to attain geometries resembling the optimized ion geometry, although they will be able to relax to some degree. Thus, the actual effects of charge on bond strength in hydrogenated amorphous silicon will be between

10

those indicated by the unoptimized (adiabatic) and optimized (vertical) rows of Table 1. They are likely to be closer to those for the unoptimized rows. Both positive and negative charges drastically weaken the bond strength of Si－Si and Si－H. The bond strength of Si－Si is weakened from 3.2 eV to 1.11 eV when Si_2H_6 is negatively charged. It is weakened to 1.6 eV when Si_2H_6 is positively charged. The bond strength of Si－H is weakened drastically from 3.9 eV to 0.98 eV when SiH_4 is negatively charged. It is weakened to 0.3 eV when SiH_4 is positively charged. The effect of charge on the bond strength can be explained by a bond order in the molecular orbital theory. A bond order, which represents the strength or stability of bond, is the number of bonding electron pairs shared by two atoms in a molecule. A bond order is defined as half the difference between the number of bonding electrons and the number of antibonding electrons as expressed by the following equation (1.1),

$$\text{Bond order} = \frac{\text{\#of bonding electrons - \#of antibonding electrons}}{2} \quad (1.1)$$

If a nanoparticle is charged negatively, electrons are added to the antibonding orbital. If a nanoparticle is charged positively, electrons are removed from the bonding orbital. Therefore,

11

both positive and negative charges would decrease the bond order and thereby weaken the bond strength. Weakening of bond strength by charge has very important implications because it means that diffusion or kinetics is enhanced. As a result, charge−induced weakening of bond strength can explain the liquid−like property of charged NPs. Therefore, these experimental and calculated results can explain the rapid kinetics of coalescence by the charge having NPs, which the enhanced chemical reactions of reactant gases even at low temperature and deposition of crystalline films at low temperature in most CVD and some PVD processes.
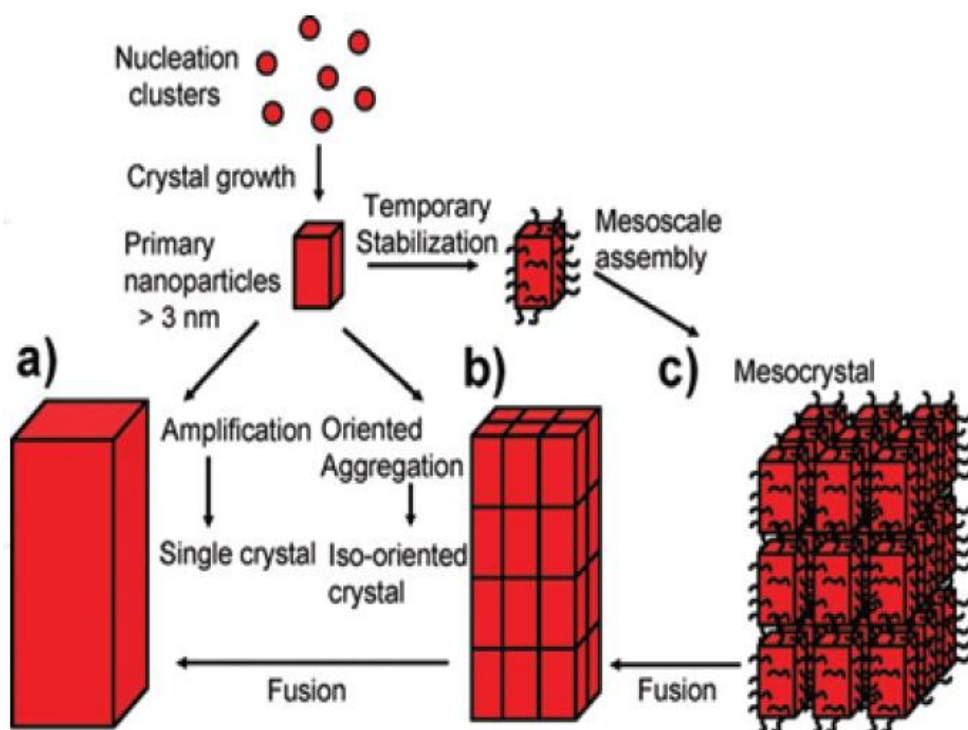
Figure 1. Schematic representation of classical and non-classical crystallization. (a) Classical crystallization. (b) oriented attachment of primary nanoparticles. (c) mesocrystal formation via self-assembly of primary nanoparticles covered with organics.
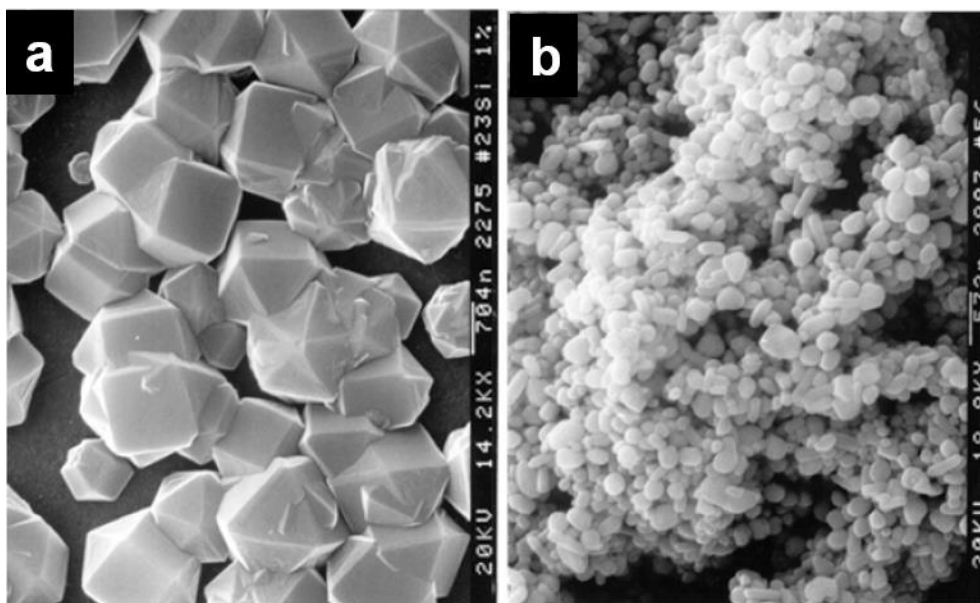
Figure 2. (a) Diamond and (b) soot grown respectively on Si and Fe substrates.
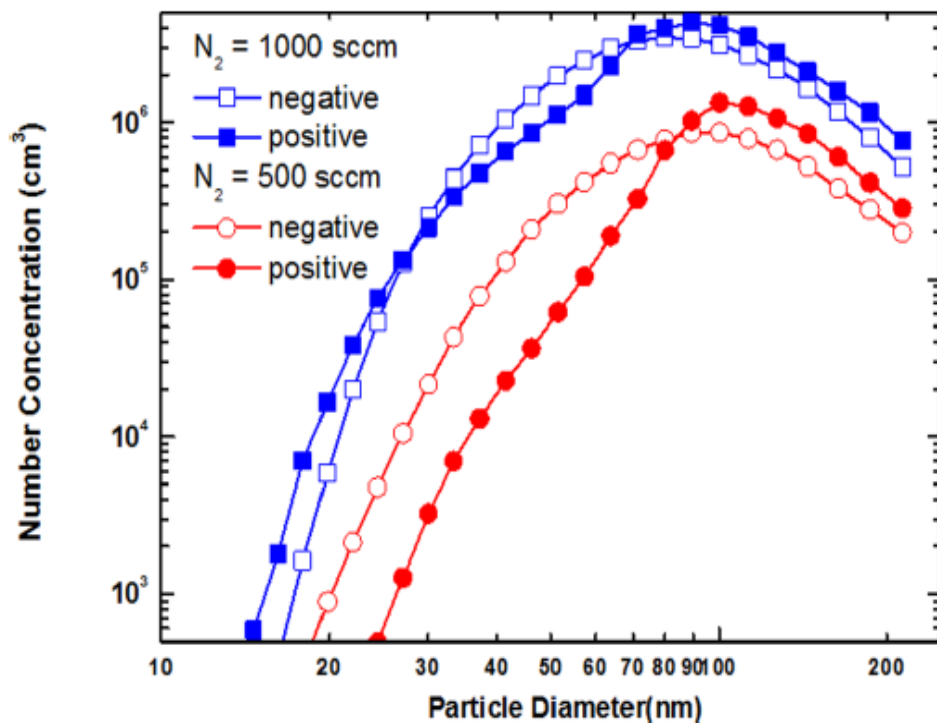
Figure 3. Number concentrations and size distributions of negatively (open) and positively (closed) charged NPs at a N_2 flow rate of 500 sccm and 1000 sccm, respectively and a reactor temperature of 900 ˚ C and a SiH_4 and H_2 flow rate of 5 sccm and 50 sccm.
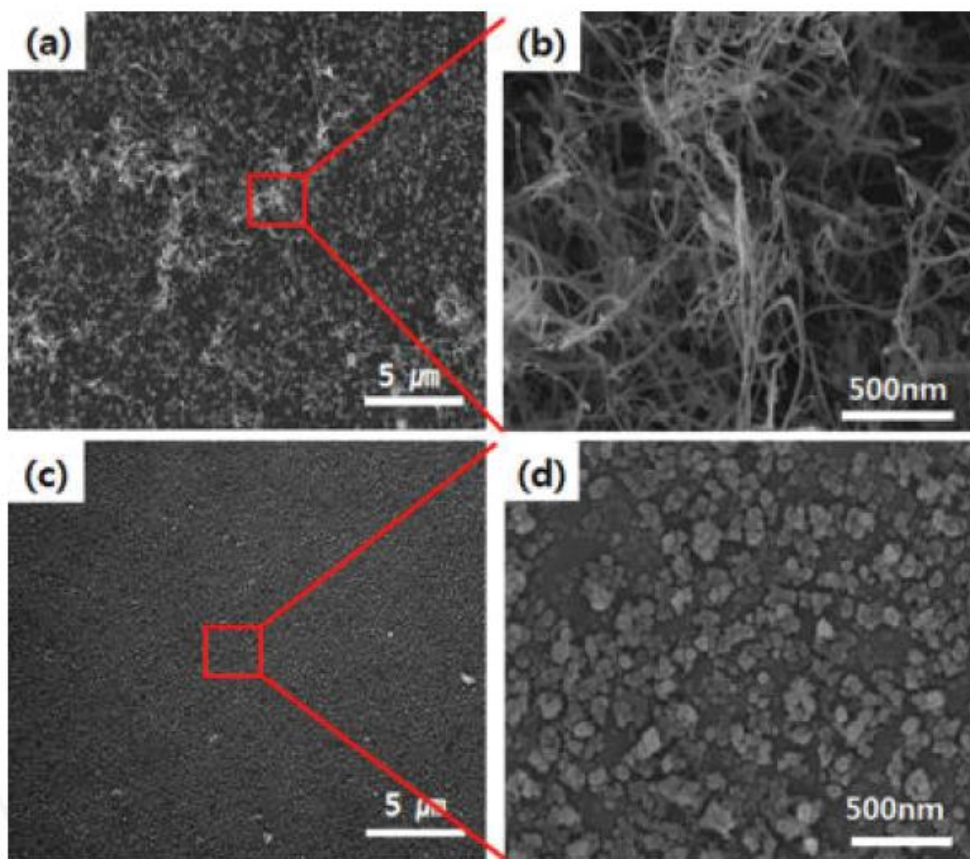
Figure 4 FESEM images of (a) low− and (b) high−magnification images of a floating substrate and (c) low− and (d) high−magnification images of a grounded substrate at a N_2 flow rate of 500 sccm.
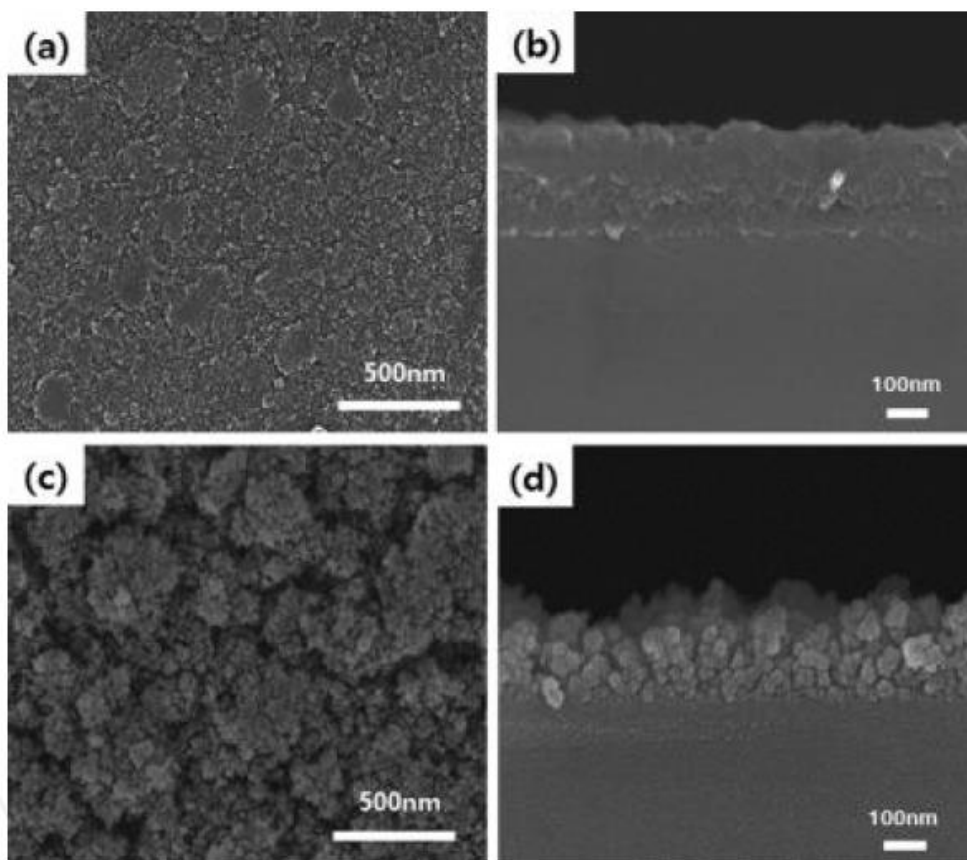
Figure 5. FESEM images of (a) top and (b) cross-section view of films deposited on a floating silicon substrate and (c) top and (d) cross-section of films deposited on a grounded silicon substrate at a N$_2$ flow rate of 1000 sccm.
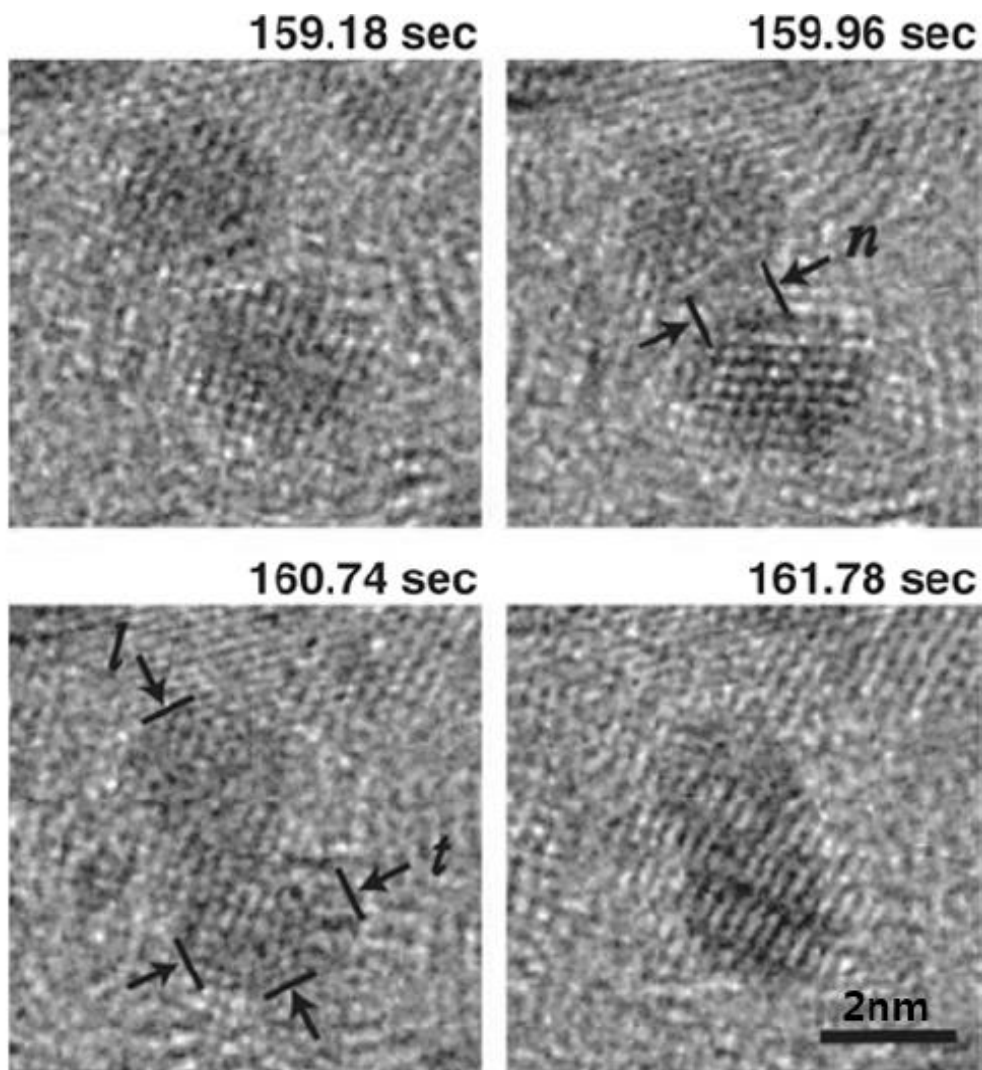
Figure 6. Pt nanocrystal coalescence dynamics. l, t, and n in the figure represent the length along the center to center direction, the thickness in vertical direction to the length and the neck diameter, respectively.

TABLE X.
Summary of Si—H and Si—Si Bond Strengths.

Compound	Si—H (eV)	Si—Si (eV)
SiH_4 (optimized)	3.9	—
SiH_4^- (optimized)	0.98	—
SiH_4^+ (optimized)	0.30	—
Si_2H_6 (optimized)	3.5	3.2
$Si_2H_6^-$ (optimized)	1.02	1.11
$Si_2H_6^+$ (optimized)	1.59	1.6
SiH_4^- (unoptimized)	1.35	—
SiH_4^+ (unoptimized)	0.09	—
$Si_2H_6^-$ (unoptimized)	1.34	1.3
$Si_2H_6^+$ (unoptimized)	1.49	1.6

Table 1. Calculation of the charge effect on Si−H and Si−Si bond strengths in hydrogenated amorphous silicon.

19

1.2. Chemical Vapor Deposition (CVD)

Chemical vapor deposition (CVD) is a vacuum deposition method used to produce high quality, high-performance, solid materials. The process is often used in the semiconductor industry to produce thin films. In typical CVD, the wafer (substrate) is exposed to one or more volatile precursors, which react and/ or decompose on the substrate surface to produce the desired deposit. Frequently, volatile by-products are also produced, which are removed by gas flow through the reaction chamber. Microfabrication processes widely use CVD to deposit materials in various forms, including: monocrystalline, polycrystalline, amorphous, and epitaxial. These materials include: silicon (dioxide, carbide, nitride, oxynitride), carbon (fiber, nanofibers, nanotubes, diamond and graphene), fluorocarbons, filaments, tungsten, titanium nitride and various high-k dielectrics.

CVD is practiced in a variety of formats. These processes generally differ in the means by which chemical reactions are initiated. First, CVD is classified by operating conditions. Atmospheric pressure CVD (APCVD), which is operating at atmospheric pressure, Low-pressure CVD (LPCVD), which is operating at sub-atmospheric pressures [28]. And reduced

pressures tend to reduce unwanted gas-phase reactions and improve film uniformity across the wafer. Ultrahigh vacuum CVD (UHVCVD) which is operating at very low pressure, typically below 10^{-6} Pa ($\approx 10^{-8}$ torr). Note that in other fields, a lower division between high and ultra-high vacuum is common, often 10^{-7} Pa. Most modern CVD is either LPCVD or UHVCVD.

Also, CVD is classified by physical characteristics of vapor. Aerosol assisted CVD (AACVD) in which the precursors are transported to the substrate by means of a liquid/ gas aerosol, which can be generated ultrasonically. This technique is suitable for use with non-volatile precursors. And direct liquid injection CVD (DLICVD) in which the precursors are in liquid form (liquid or solid dissolved in a convenient solvent). Liquid solutions are injected in a vaporization chamber towards injectors (typically car injectors). The precursor vapors are then transported to the substrate as in classical CVD. This technique is suitable for use on liquid or solid precursors. High growth rates can be reached using this technique.

In addition, CVD is classified by type of substrate heating. Hot wall CVD in which the chamber is heated by an external power source and the substrate is heated by radiation from the heated chamber walls. And cold wall CVD in which only the

substrate is directly heated either by induction or by passing current through the substrate itself or a heater in contact with the substrate. The chamber walls are at room temperature.

At last, there is the type of CVD assisted by plasma methods. Plasma−Enhanced CVD (PECVD) utilizes plasma to enhance chemical reaction rates of the precursors [29]. PECVD processing allows deposition at lower temperatures, which is often critical in the manufacture of semiconductors. The lower temperatures also allow for the deposition of organic coatings, such as plasma polymers, that have been used for nanoparticle surface functionalization [30]. And remote plasma−enhanced CVD (RPECVD) is similar to PECVD except that the wafer substrate is not directly in the plasma discharge region. Removing the wafer from the plasma region allows processing temperatures down to room temperature. Low−Energy Plasma−Enhanced chemical vapor deposition (LEPECVD) is employing a high density, low energy plasma to obtain epitaxial deposition of semiconductor materials at high rates and low temperatures. Atomic−layer CVD (ALCVD) – Deposits successive layers of different substances to produce layered, crystalline films. Combustion Chemical Vapor Deposition (CCVD) – Combustion Chemical Vapor Deposition or flame pyrolysis is an open−atmosphere, flame−based technique for

depositing high-quality thin films and nanomaterials. Hot filament CVD (HFCVD) – also known as catalytic CVD (Cat-CVD) or more commonly, initiated CVD (iCVD), this process uses a hot filament to chemically decompose the source gases [31]. The filament temperature and substrate temperature thus are independently controlled, allowing colder temperatures for better absorption rates at the substrate and higher temperatures necessary for decomposition of precursors to free radicals at the filament [32]. Hybrid Physical-Chemical Vapor Deposition (HPCVD) – This process involves both chemical decomposition of precursor gas and vaporization of a solid source. Metalorganic chemical vapor deposition (MOCVD) – This CVD process is based on metalorganic precursors. Rapid thermal CVD (RTCVD) – This CVD process uses heating lamps or other methods to rapidly heat the wafer substrate. Heating only the substrate rather than the gas or chamber walls helps reduce unwanted gas-phase reactions that can lead to particle formation. Photo-initiated CVD (PICVD) uses UV light to stimulate chemical reactions. It is similar to plasma processing, given that plasmas are strong emitters of UV radiation. Under certain conditions, PICVD can be operated at or near atmospheric pressure [33]. Laser Chemical vapor deposition (LCVD) – This CVD process uses lasers to heat spots or lines

on a substrate in semiconductor applications. In MEMS and in fiber production the lasers are used rapidly to break down the precursor gas, process temperature can exceed 2000 °C, to build up a solid structure in much the same way as laser sintering based 3-D printers build up solids from powders.

CVD is commonly used to deposit conformal films and augment substrate surfaces in ways that more traditional surface modification techniques are not capable of. CVD is extremely useful in the process of atomic layer deposition at depositing extremely thin layers of material. A variety of applications for such films exist. Gallium arsenide is used in some integrated circuits (ICs) and photovoltaic devices. Amorphous polysilicon is used in photovoltaic devices. Certain carbides and nitrides confer wear-resistance [34]. Polymerization by CVD, perhaps the most versatile of all applications, allows for super-thin coatings which possess some very desirable qualities, such as lubricity, hydrophobicity and weather-resistance to name a few [35]. CVD of metal-organic frameworks, a class of crystalline nanoporous materials, has recently been demonstrated [36]. Applications for these films are anticipated in gas sensing and low-k dielectrics CVD techniques are adventageous for membrane coatings as well, such as those in desalination or water treatment, as these

coatings can be sufficiently uniform (conformal) and thin that they do not clog membrane pores [37].

1.3 Physical Vapor Deposition (PVD)

Physical vapor deposition (PVD) describes a variety of vacuum deposition methods which can be used to produce thin films and coatings. PVD is characterized by a process in which the material goes from a condensed phase to a vapor phase and then back to a thin film condensed phase. The most common PVD processes are sputtering and evaporation. PVD is used in the manufacture of items which require thin films for mechanical, optical, chemical or electronic functions. Examples include semiconductor devices such as thin film solar panels [38] aluminized PET film for food packaging and balloons [39] and titanium nitride coated cutting tools for metalworking. Besides PVD tools for fabrication, special smaller tools (mainly for scientific purposes) have been developed [40]. The source material is unavoidably also deposited on most other surfaces interior to the vacuum chamber, including the fixturing used to hold the parts.

Advantages are as follows. PVD coatings are sometimes harder and more corrosion resistant than coatings applied by the

electroplating process. And most coatings have high temperature and good impact strength, excellent abrasion resistance and are so durable that protective topcoats are almost never necessary. Also, it has ability to utilize virtually any type of inorganic and some organic coating materials on an equally diverse group of substrates and surfaces using a wide variety of finishes. PVD is environmental friendly than traditional coating processes such as electroplating and painting. Disadvantages are as follows. Specific technologies can impose constraints; for example, line−of−sight transfer is typical of most PVD coating techniques, however there are methods that allow full coverage of complex geometries. And a few PVD technologies typically operate at very high temperatures and vacuums, requiring special attention by operating personnel. Also, it requires a cooling water system to dissipate large heat loads.

1.3.1 Sputter deposition

Sputter deposition is a PVD method of thin film deposition by sputtering [41]. This involves ejecting material from a target that is a source onto a substrate such as a silicon wafer. In Figure 7, the processes occur when the target surface is

hit by an ion. The ion can be reflected and can be neutralized immediately afterwards. This scattering process is the basis of an analysis technique called ion scattering spectroscopy. The ion bombardment can eject and electron from the target, and this process is called secondary electron. The ion can penetrate into the target. This process is known as ion implantation, and it is widely employed in the technology of integrated circuits for selectively doping silicon wafers. It allows for the control of the impurity atoms' depth and quantity. The ion can cause structural changes in the target material. These changes can not only simple vacancies and interstitial defects but also major lattice defects, which can provoke changed in the target composition. Finally, the ion impact can originate a series of a collisions among the target atoms. This ejection process is called sputtering. This continuous current glow discharge that originates the energetic particles that support the sputtering process can be obtained by applying a potential difference (voltage) between two electrodes in the presence of a gas kept at low pressure inside a vacuum chamber. The voltage can be delivered by a continuous current power supply that provide tens of thousands of volts, depending on the equipment configuration. In this process, an electric field is formed between the

electrode separated by a distance d ad having a potential difference V; this will generate an electric current in the rarefied gas, due to the presence of electrons and ions formed by processes such as ionization by cosmic rays, thermionic emission, and collisions between particles, as shown in Figure 8.

Sputtered atoms ejected from the target have a wide energy distribution, typically up to tens of eV (100,000 K). The sputtered ions (typically only a small fraction of the ejected particles are ionized; on the order of 1 percent) can ballistically fly from the target in straight lines and impact energetically on the substrates or vacuum chamber (causing resputtering). Alternatively, at higher gas pressures, the ions collide with the gas atoms that act as a moderator and move diffusively, reaching the substrates or vacuum chamber wall and condensing after undergoing a random walk. The entire range from high-energy ballistic impact to low-energy thermalized motion is accessible by changing the background gas pressure. The sputtering gas is often an inert gas such as argon. For efficient momentum transfer, the atomic weight of the sputtering gas should be close to the atomic weight of the target, so for sputtering light elements neon is preferable, while for heavy elements krypton or xenon are used. Reactive

gases can also be used to sputter compounds. The compound can be formed on the target surface, in-flight or on the substrate depending on the process parameters. The availability of many parameters that control sputter deposition make it a complex process, but also allow experts a large degree of control over the growth and microstructure of the film.

An important advantage of sputter deposition is that even materials with very high melting points are easily sputtered while evaporation of these materials in a resistance evaporator or Knudsen cell is problematic or impossible. Sputter deposited films have a composition close to that of the source material. The difference is due to different elements spreading differently because of their different mass (light elements are deflected more easily by the gas) but this difference is constant. Sputtered films typically have a better adhesion on the substrate than evaporated films. A target contains a large amount of material and is maintenance free making the technique suited for ultrahigh vacuum applications. Sputtering sources contain no hot parts (to avoid heating they are typically water cooled) and are compatible with reactive gases such as oxygen. Sputtering can be performed top-down while evaporation must be performed

bottom-up. Advanced processes such as epitaxial growth are possible.

Some disadvantages of the sputtering process are that the process is more difficult to combine with a lift-off for structuring the film. This is because the diffuse transport, characteristic of sputtering, makes a full shadow impossible. Thus, one cannot fully restrict where the atoms go, which can lead to contamination problems. Also, active control for layer by layer growth is difficult compared to pulsed laser deposition and inert sputtering gases are built into the growing film as impurities.

1.3.2 Direct current (DC) sputtering

This system comprises of a pair of planar electrodes. One of the electrodes (cathode) is the target and the substrate, mounted on the anode, is grounded, as can be seen in the Figure 9 [42]. The outer face of the cathode is cooled by water. The sputtering system chamber is kept at a pressure P and a voltage of a few kilovolts is applied between the electrodes in order to initiate a glow discharge. The positive argon ions present in the plasma will be accelerated towards the cathode, causing the sputtering of target atoms, which will

cause the deposition of a thin film on the substrate. The cathode (target) in DC diode systems must be conductive since and insulator surface that will prevent the ion bombardment on the target surface, interrupting the sputtering process.

As using adequate magnets behind the target, the electrons can remain close to the target surface, and thus increase the electron density by magnetic field, which this system is called DC magnetron sputtering in Figure 10. The high flux of electrons generates high density plasma, from which the ions can be extracted in order to bombard the target. This electrons confinement by the magnetic field enhances the ionization probability of a neutral molecule of the gas by several magnitude orders. This increase in the ion density enhances the sputter yield significantly and, the deposition rate on the substrate. This configuration allows for sputtering at low pressures (<5 mTorr).

1.3.3 Radio frequency (RF) sputtering

When an insulator target is employed, the glow discharge will not be sustained due to the immediate formation of a positively charged surface on the exposed face of the

insulator material. In order to maintain the slow discharge using an insulator target, the DC power supply has to be replaced by a RF power supply, and the system called a RF sputtering system. When a RF potential with a high peak－to－peak voltage is usually coupled to an electrode, an alternating positive and negative voltage appears at the electrode surface. During part of each half cycle, the potential is such that accelerates the ions towards the surface with enough energy to sputter. In the other half cycle, the electrons that reach the target surface prevent the formation of a charge barrier. This system requires an impedance－matching network between the power supply and the chamber. The impedance of the RF source is 50 ohm, and the discharge impedance is in the range of 1 ～ 10 k－ohm. In this system, the current density is given as following equation,

$$I_s \cong CdV/dt \qquad\qquad (1.2)$$

Where C is the capacitance between the plasma and the target and dV/ dt represent the variation with time of the target surface potential. From Eq (4) we can observe that the ion current in the cathode increases with the increase of frequency. In commercial systems, the applied frequency is

13.56MHz.

1.4 Purpose of this study

As mentioned above, the theory of charged nanoparticles has been demonstrated by calculations and experimental proofs. However, the theory of charged nanoparticles has been mostly studied in CVD systems. Although some PVD systems, such as a thermal evaporator, have been studied, few studies have been conducted on theory of charged nanoparticles in PVD systems. However, even in PVD systems, the existence of charged nanoparticles generated in the gas phase during the process could be sufficiently predicted, and thus, a study on this is necessary. For example, plasma, which is commonly used in PVD systems is widely known to have charged particles such as ions, electrons and neutral species that could be ionized by collision with high energy electrons and ions. Among these PVD systems, sputtering is very popular and is one of the most widely used methods for thin film deposition.

Therefore, the research purpose during the Ph. D. course is to confirm the possibility of generation of charged nanoparticles using RF magnetron sputtering, PVD system, and to investigate the effect of the charged nanoparticles on thin

film deposition. Furthermore, the study suggests that the theory of charged nanoparticle is suitable for explanation for the general thin film deposition behavior.
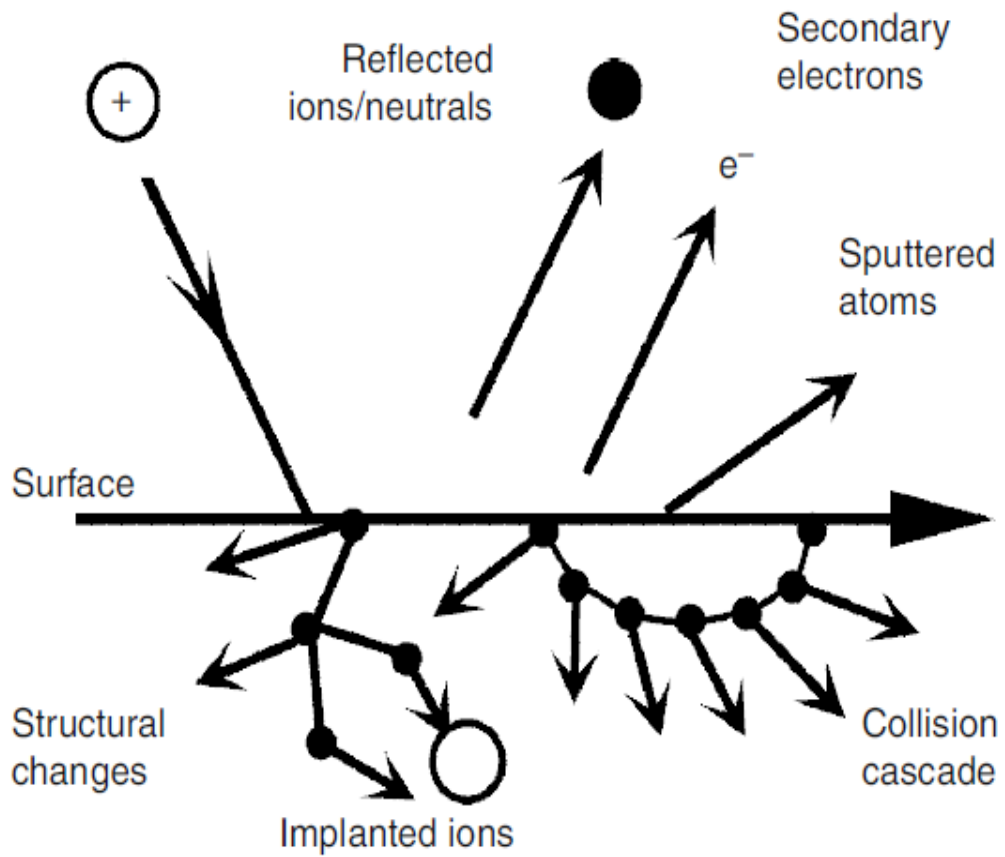
Figure 7. Phenomena on the target surface by bombardment of energetic particles.
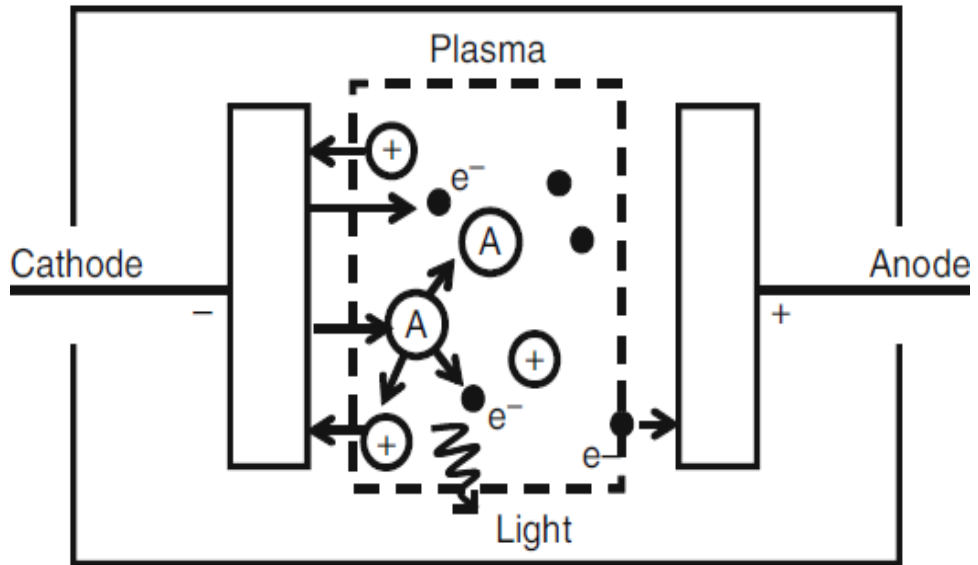
Figure 8. Glow discharge formation inside the vacuum chamber for generating the energetic particles.
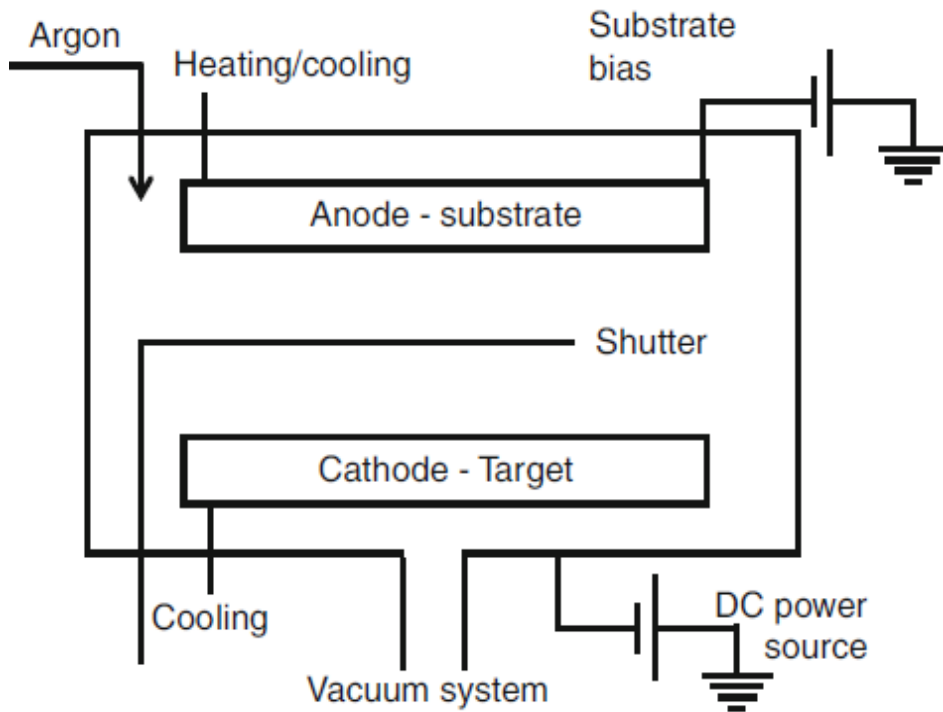
Figure 9. Schematics of a conventional DC sputtering system.
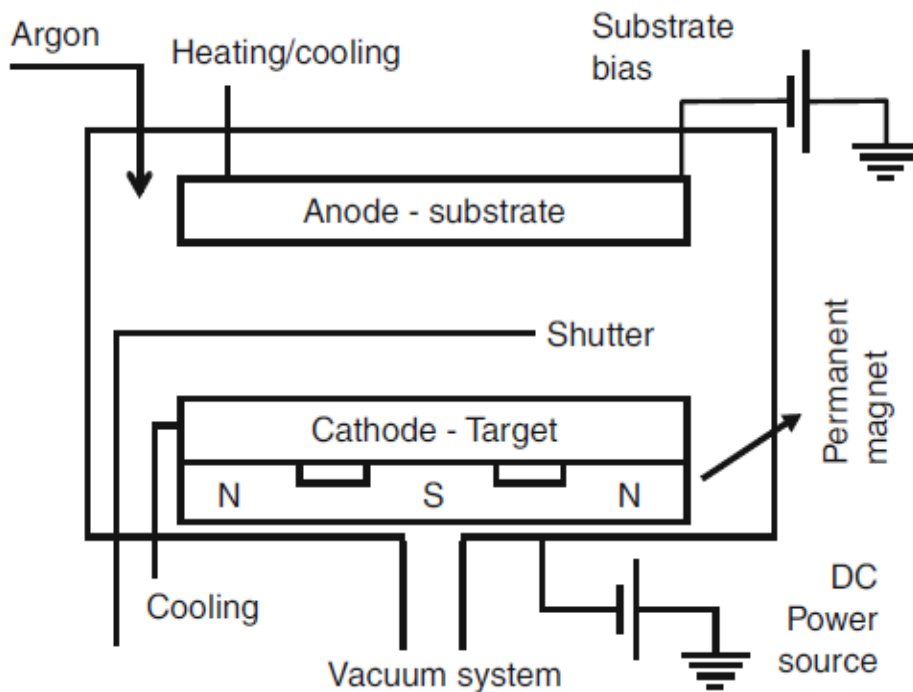
Figure 10. Schematics of a DC magnetron sputtering system.

Chapter 2.

Generation of charged Ti nanoparticles and their deposition behavior with substrate bias during RF magnetron sputtering

2.1. Introduction

Titanium (Ti) thin films are widely used in biomedical applications and microelectronics because of their outstanding properties such as good biocompatibility, excellent thermal and chemical stability [43−48]. Ti films are broadly prepared using sputtering, which is a well−established technique in industry to deposit thin films with high reproducibility and growth rate [49−55].

Meanwhile, the deposition process of thin films has been understood based on the classical crystallization that thin films grow by the building block of atoms, ions and molecules. However, there have been several puzzling phenomena that

cannot be explained by the classical crystallization mechanism. Recently, many researchers have reported experimental evidence that the thin films grow by the building block of NPs, which has been called 'non-classical crystallization' [56-62].

Hwang et al. have extensively studied non-classical crystallization in a CVD system [63]. They suggest that the NPs having an electric charge are spontaneously generated in the gas phase in a conventional CVD process and become the building blocks of thin films. The charge carried by the NPs plays an important role in the deposition of crystalline thin films and in the synthesis of nanostructures such as nanorod and tetrapod [64-69]. They called this new crystal growth mechanism 'theory of charged NPs (TCN)'. According to TCN, neutral NPs form a porous structure by random Brownian coagulation, whereas charged NPs produce a dense film, resulting from the orderly manner of deposition by self-assembly. On landing on the surface, charged NPs undergo liquid-like coalescence or epitaxial recrystallization and result in dense and crystalline structures. The liquid-like coalescence implies that the bond strength of NPs might be weakened by the charge. Indeed, Clare et al. [27] reported that the bond strength of Si-H and Si-Si is weakened by the charge in silane (SiH_4) and disilane (Si_2H_6) molecules by the ab initio

calculation. Also, these understandings of TCN have been demonstrated experimentally in many CVD systems. For instance, a homoepitaxial Si film on the Si substrate was deposited by applying the negative substrate bias at a low substrate temperature of 550°C during plasma enhanced CVD [70] and a high crystalline and dense Si film was obtained by controlling the behavior of Si charged NPs during inductively coupled plasma CVD [71].

A few studies have utilized NPs for thin film deposition in PVD systems. Sahu et al. [72] enhanced the properties of indium tin oxide (ITO) films by inducing the generation of crystalline NPs during a modified RF sputtering system with 3-D confined magnetron source. Hayasaki et al. [73] also obtained epitaxial yttrium barium copper oxide (YBa_2CuO_{7-x}) films using nano-sized clusters during thermal plasma flash evaporation. However, these studies did not concern the presence and the role of the charge of NPs carefully.

In this chapter, the generation of charged NPs and their effects on film deposition during the conventional RF sputtering system using a Ti target were carefully investigated. The generation of Ti NPs and their polarity were confirmed by applying the electric bias to commercial amorphous carbon membranes for transmission electron microscopy (TEM). The

effects of charged Ti NPs on the film deposition were examined by applying the electric bias to p-type Si (100) substrates. Characteristics of the Ti NPs and films were analyzed by TEM, field-emission scanning electron microscopy (FESEM) and x-ray reflectivity (XRR).

2.2. Experimental methods

Figure 11(a) shows schematics of the RF sputtering system using a Ti target. The distance between the Ti target and a sample stage was 7 cm. An amorphous carbon TEM membrane (Ted Pella, Inc.) for capturing NPs and a p-type Si substrate for film deposition were placed on a steel plate, which was electrically isolated with the grounded sample stage in order to apply the electric bias on the steel plate. A grounded mesh in Figure 11(b) was installed 2 mm above the steel plate to prevent the electric bias of the steel plate from interfering with the plasma condition. The electric field generated between the grounded mesh and steel plate would interact with charged NPs, if any. A round-shaped shutter with 5 cm diameter was installed 5 mm above the grounded mesh in order to control the exposure time for capturing NPs or the deposition of film. In other words, the plasma flux was blocked when the shutter was

closed, and the capturing or deposition started shortly after the shutter opened.

Ar gas pressure, RF power and substrate temperature were 20mTorr, 160W and room temperature, respectively, for all experiments. To confirm the existence of Ti charged NPs, the Ti NPs were captured on the TEM membrane for 30 sec at various electric biases of −70, 0, +5, +15 and +30V. Also, to confirm the effect of Ti charged NPs on the actual deposition process, Ti thin films were deposited on Si substrates for 30 min at −70, 0 and +30V under the same condition as capturing NPs.

To stabilize the plasma condition, the capturing NPs and film deposition processes were conducted 30 sec after the plasma is turned on. During this stabilizing time of 30 sec, the TEM membrane and the Si substrate were perfectly screened by the shutter from the plasma.

The captured Ti charged NPs were analyzed by TEM (FEI, Tecnai F20). The microstructure of the Ti films was investigated by SEM and TEM. The density of the films was calculated by measuring critical angles of XRR.

2.3. Results and Discussion

A. Capturing charged NPs during Ti RF sputtering

Charged NPs, if any, were expected to interact with the electric field generated between the grounded mesh and the steel plate. In Figure 12(a)−(e), scanning transmission electron microscope (STEM) images show the white dots with various steel plate biases of −70, 0, +5, +15 and +30V, respectively. These white dots were confirmed to be titanium dioxide (TiO_2) NPs, which will be described further in Figure 15. The number density of NPs increased by increasing the negative bias from 0V to −70V in Figure 12(a) and 12(b). In contrast, it decreased by increasing the positive bias from 0V to +30V in Figure 12(c)−(e), which shows that the NPs were positively charged since they were attracted to the TEM membrane when the negative bias was applied, whereas they were repelled when the positive bias was applied. The more positive bias was applied, the more positively charged NPs were repelled based on the energy distribution of NPs. Figure 13 is schematics to describe the behavior of the sputtered species at the negative and the positive substrate bias, respectively.

The NPs were not observed on the TEM membrane at

+30V as shown in Figure 12(e). All positively charged NPs were expected to be repelled. On the other hand, negatively charged NPs were expected to be blocked by the grounded mesh like electrons due to the potential difference between plasma and the grounded mesh. The grounded mesh has more negative potential with respect to plasma since plasma has always the most positive potential in the chamber. Therefore, any negatively charged particle that does not have enough energy to overcome the potential difference between plasma and the grounded mesh could not come to the TEM membrane through the grounded mesh. Thus, negatively charged NPs passing through the grounded mesh were expected to be hardly observed on the TEM membrane.

In the case of neutral NPs, there are two possibilities as to the absence of NPs on the TEM membrane at +30V. One possibility is that there were no neutral NPs that came to the TEM membrane since the neutral NPs should be observed regardless of the sign of the applied bias. The other possibility is that the neutral NPs landed on the TEM membrane but could not be observed because of their too small size to be detected by high−resolution transmission electron microscopy (HRTEM). To ascertain these two possibilities, Ti thin films were deposited for a longer time under the same conditions as

capturing the charged NPs, which will be discussed in Section B.

Figure 14 shows HRTEM images and fast Fourier transform (FFT) information of the NPs captured at -70V and 0V. The majority of the captured NPs had the average size of ~5 nm and d-spacing of ~0.217 nm, indicating that the charged NPs were TiO_2 with the (220) crystal plane. This is because Ti becomes oxidized easily. Ti NPs might turn into TiO_2 NPs immediately after they were taken out of the vacuum chamber and exposed to air [74].

B. Ti thin film deposition

Ti films were deposited on Si substrates for 30 min under the condition where the bias of -70, 0 and $+30$V was applied to the steel plate substrate holder. Cross-section SEM images of these films are shown in Figure 15. Compared to the Ti film at 0V, a thicker film was obtained at -70V, whereas a thinner film was obtained at $+30$V. This should be attributed to the difference of the number density of positively charged Ti NPs as shown in Figure 12.

In the case of $+30$V, a 92 nm thick Ti film was deposited although no NPs were observed as shown in Figure 12(e). If neutral NPs did not exist, the Ti film would be deposited only

by neutral atoms and should have the highest crystallinity and density under bias conditions of -70, 0 and $+30V$. On the other hand, if neutral NPs were not observed because of their invisibly small size as discussed above, the Ti film would be deposited by the invisibly small neutral Ti NPs as well as atoms and should have low crystallinity and density. Jeon et al. [27] reported that the film deposited by a high fraction of neutral clusters showed a rough surface morphology and a fractal structure whereas the film with a high fraction of charged clusters showed a smooth morphology and high quality during copper thermal evaporation. Therefore, it is necessary to analyze crystallinity and density of the films deposited at -70, 0 and $+30V$ to distinguish whether the film grows mainly by neutral atoms or clusters.

Figures 16 shows XRD data of the films deposited at -70, 0 and $+30V$. In Figure 16, the films deposited at $-70V$ and $0V$ mainly show XRD peaks with the (100) and the (002) orientation of Ti, respectively. However, the film deposited at $+30V$ does not show any clear XRD peak, which means that the film was amorphous.

Figures 17(a)$-$(c) and 17(d)$-$(f) show respectively low and high magnification HRTEM images of the films deposited at -70, 0 and $+30V$. In Figure 17(d)$-$(f), the films deposited at

−70V and 0V show lattice fringe images of the higher contrast and clearer FFT images in the right bottom inset than that deposited at +30V. The film deposited at +30V had amorphous regions as marked by the ovals in Figure 17(f). Moreover, as shown in Figure 18(a)−(c), the films deposited at −70V and 0V had clear diffraction patterns, whereas that deposited at +30V had an obscure and ring−shaped pattern.

Considering the analysis of XRD, HRTEM and diffraction pattern images, it can be concluded that the films deposited at −70V and 0V had higher crystallinity than that deposited at +30V. Therefore, as mentioned above, we confirm the possibility that the film deposited at +30V grow mainly by neutral clusters, rather than by neutral atoms. To verify this possibility further, the density of the films was analyzed.

Figure 19 corresponds to the first 0.7 degrees of XRR graphs of the films deposited at −70, 0 and +30V, which show the critical angle of the films at the inflection point of the graphs. The critical angle of the films deposited at −70, 0 and +30V were 0.31°, 0.28° and 0.25°, respectively. The density of the film was theoretically calculated using equation (1),

$$\alpha_C \approx \sqrt{\frac{r_0 \lambda^2}{\pi} N_A \frac{(Z + f')}{A} \rho} \qquad (2.1)$$

where α_c is the critical angle, r_0 is the classical electron radius, λ is the wavelength of CuKα1, N_A is Avogadro's number, Z is the atomic number of Ti, f' is the real part of the dispersion coefficient, A is the atomic weight of Ti and ρ is the density of the films. Theoretically calculated densities of films deposited at −70, 0 and +30V were 4.974, 4.058 and 3.499 g/ cm^3, respectively. Table 2 shows the summarized characteristics of the films. It is noted that the film deposited at +30V showed the lowest crystallinity and density. Considering these results, it is confirmed that the deposition of the film at +30V was contributed mainly by the invisibly small neutral NPs and neutral atoms. Therefore, the neutral NPs were expected to land on the substrate although they were not observed by TEM due to their small size. Neutral atoms would also deposit on the substrate, but it seems that they did not significantly improve the film quality. If the film at +30V was deposited solely atom by atom like atomic layer deposition (ALD), it should have an extraordinarily high crystallinity and density, which may exceed the properties of the films deposited at −70V and 0V.

On the other hand, the highest crystallinity and density of the film deposited at −70V were attributed to the positively charged NPs, which came down through the grounded mesh, and were accelerated toward the negatively biased substrate

and formed the dense film. Therefore, charged NPs played an important role in growing the highly crystalline and dense film at room temperature in the RF sputtering process.

2.4. Conclusion

Generation of charged NPs and their effect on film deposition as the substrate bias were discussed during RF sputtering system. The NPs were captured on the TEM membrane with the electric bias of −70, 0, +5, +15 and +30V at room temperature for 30 sec. The number density of NPs increased with increasing the negative bias (−70V), whereas decreased with increasing the positive bias (+5 and +15V) and became negligible at +30V, which indicated that the majority of NPs were positively charged.

Ti thin films were also deposited on Si substrates with the bias of −70, 0 and +30V at room temperature for 30 min. The thickness of the Ti films of −70, 0 and +30V were 180, 146 and 92 nm while the density of these were 4.974, 4.058 and 3.499 g/ cm^3, respectively. The film at −70V had the highest thickness, density, and crystallinity, which was attributed to the attraction of the positively charged NPs. In contrast, the Ti film at +30V exhibited the lowest crystallinity and this was

attributed to the deposition of minute－sized neutral NPs. These results described the fact that the charged NPs could improve the film quality even at room temperature. Conclusively, in RF sputtering, the generation charged NPs were confirmed and the charged NPs could be a critical parameter to deposit high quality films.

a

13.56 MHz

Target (Ti)

D_{TM}: 7 cm

Shutter

Grounded mesh

D_{MS}: 1~2 mm

Sub.

F

Sample stage

Bias device

b

26 mm

15 mm

5 mm

$\phi_{aperture}$ 0.15 mm
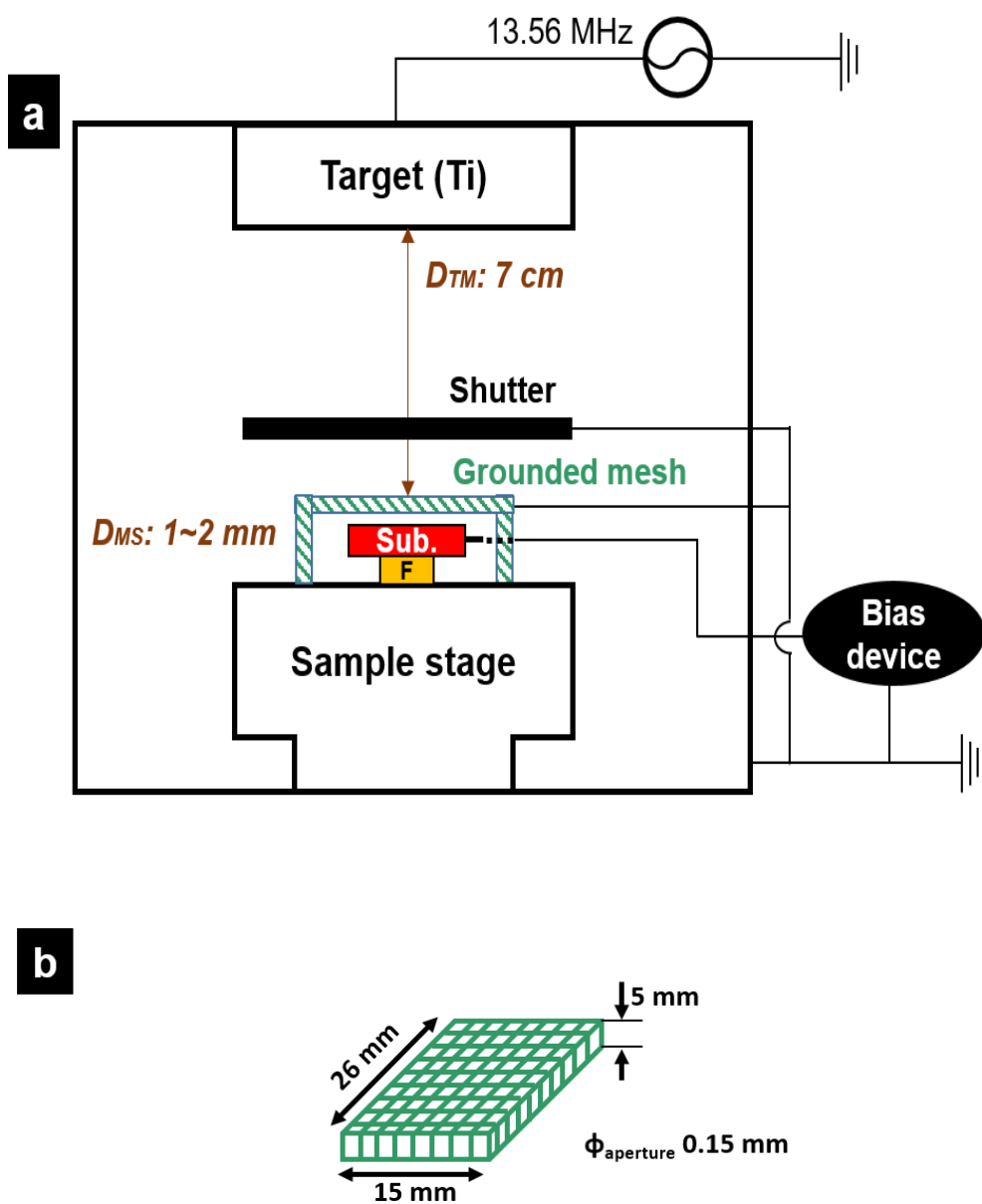
Figure 11. Schematics of RF sputtering system a) main chamber b) grounded mesh.
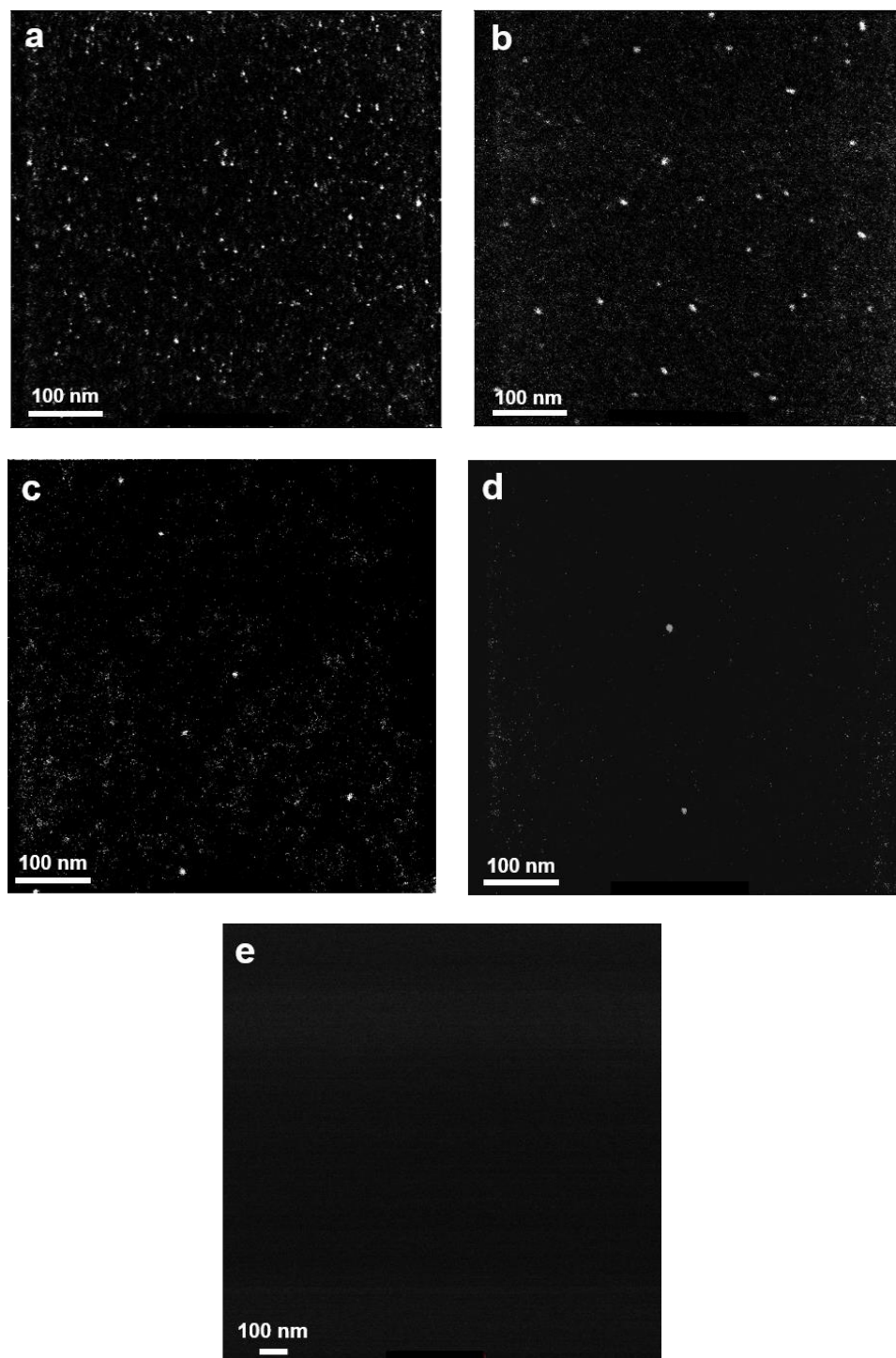
Figure 12. STEM images of NPs captured on amorphous carbon TEM membranes at the electric bias of a) −70V b) 0V c) +5V d) +15V and e) +30V.
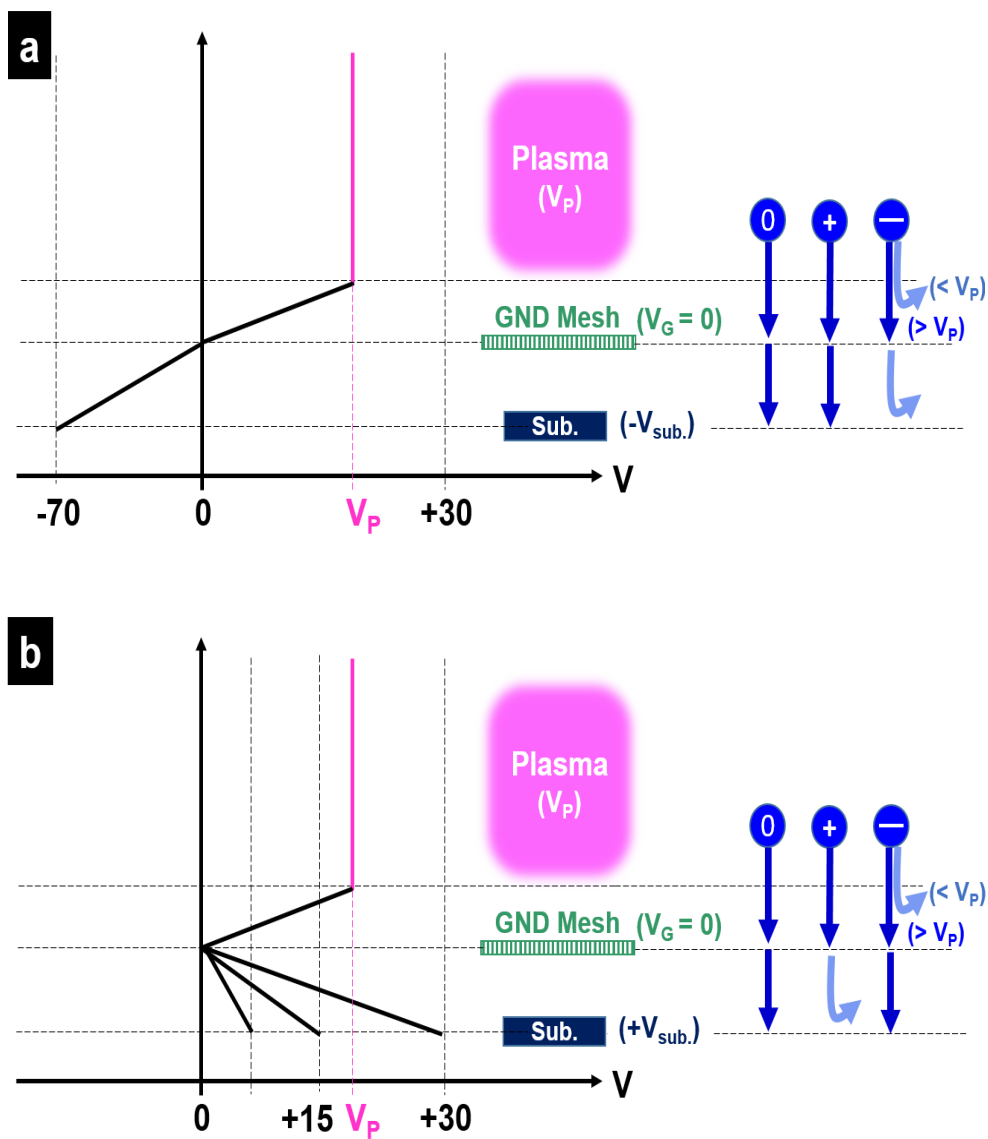
Figure 13. Schematics of the sputtered species behavior as substrate bias. a) Negative bias and b) positive bias.
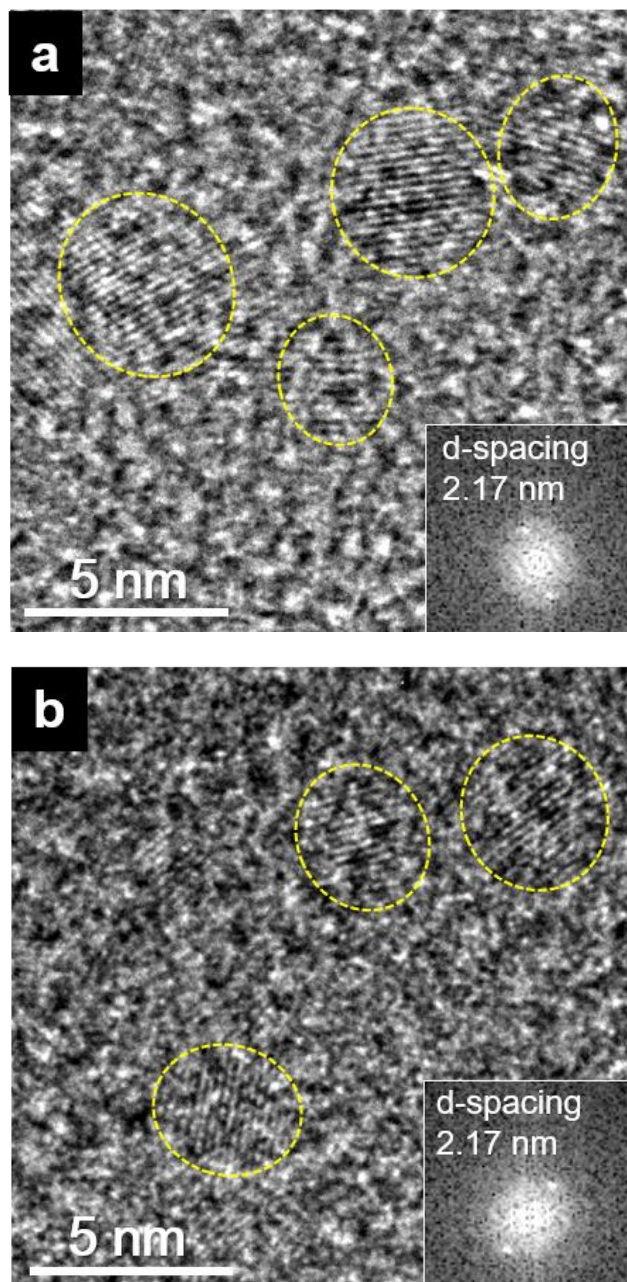
Figure 14. HRTEM images and fast Fourier transform (FFT) information (inset of the lower right in the image) with d-spacing value of NPs at the electric bias with a) −70V and b) 0V.
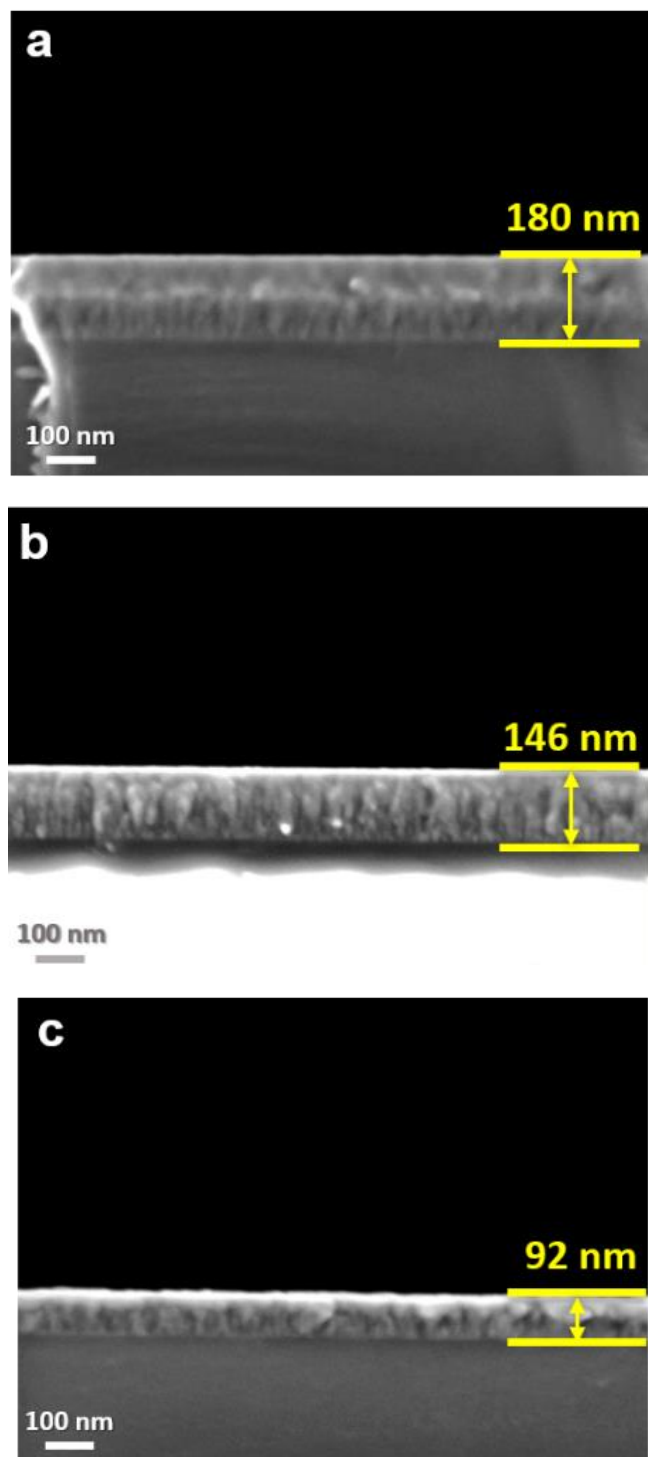
Figure 15. SEM images of Ti films deposited on Si substrates at the electric bias of a) −70V b) 0V and c) +30V.
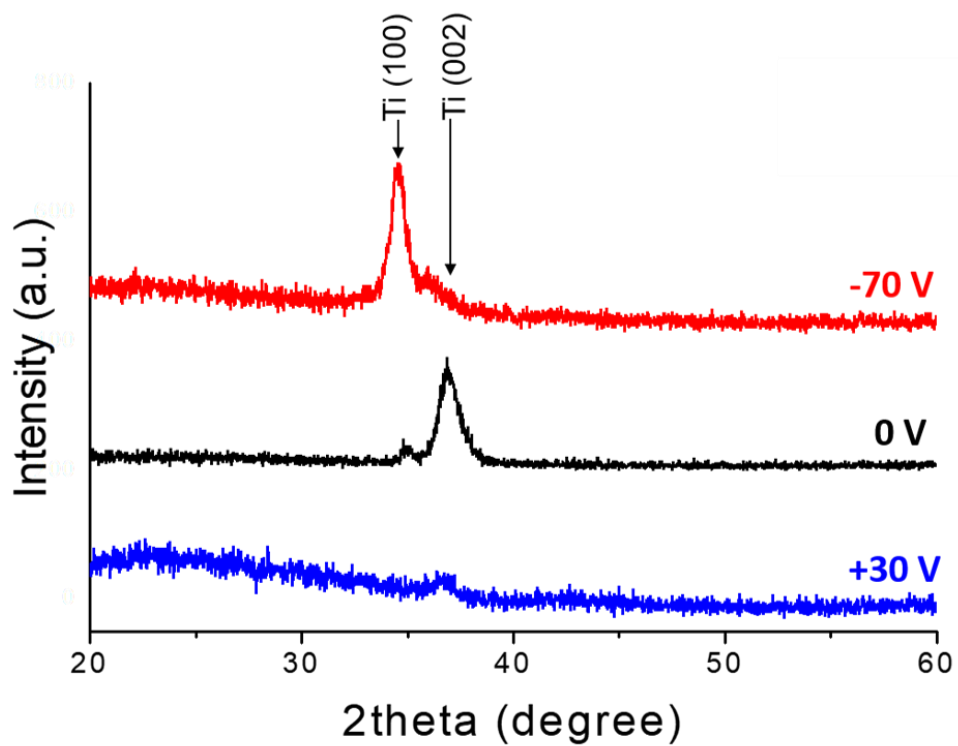
Figure 16. XRD data of the Ti films deposited at the electric bias of −70V, 0V and +30V.
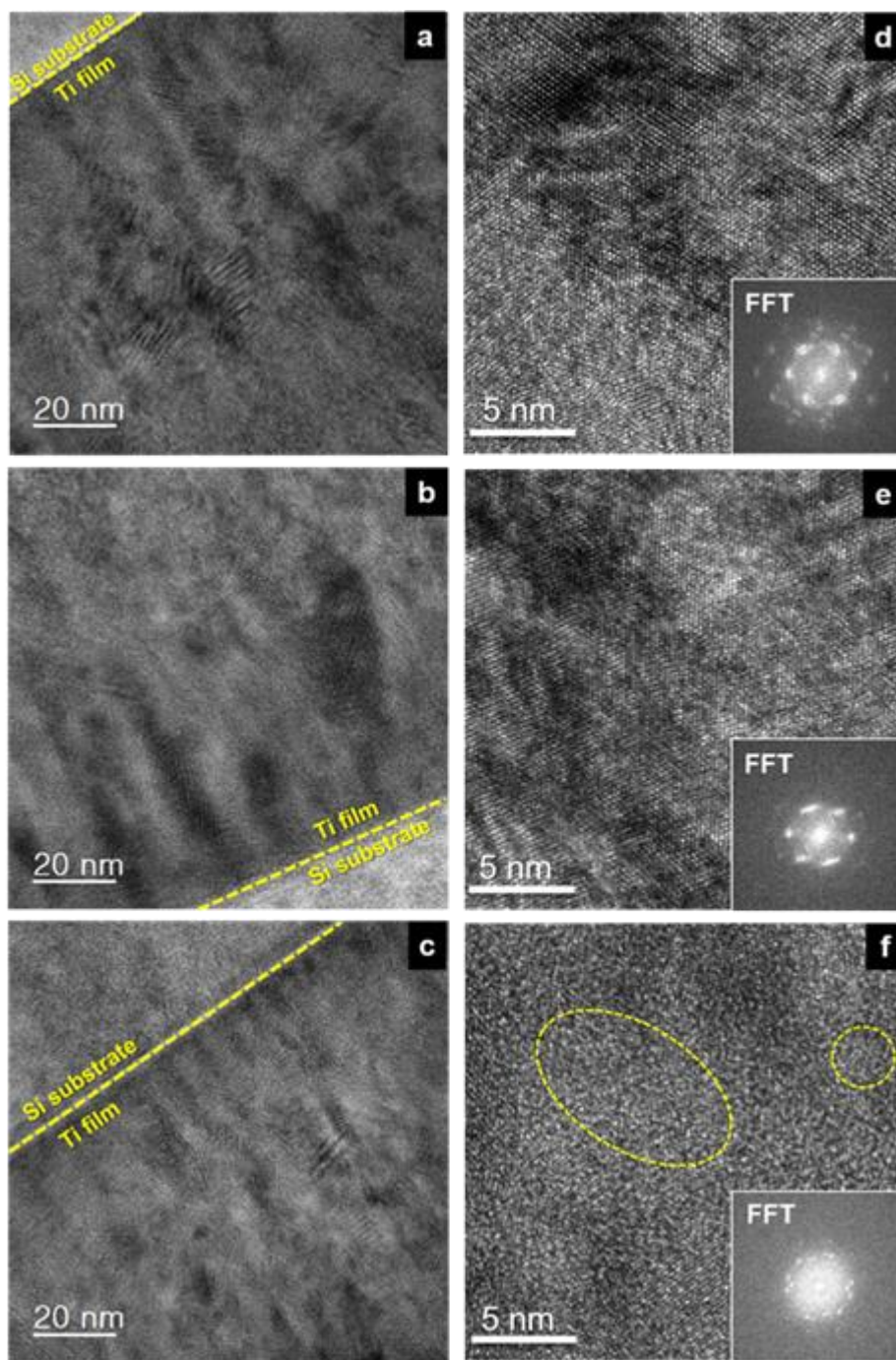
Figure 17. HRTEM images of a)−c) low magnification and d)− f) high magnification with FFT information of the Ti films deposited on Si substrates at the electric bias of a), d) −70V b), e) 0V and c), f) +30V.
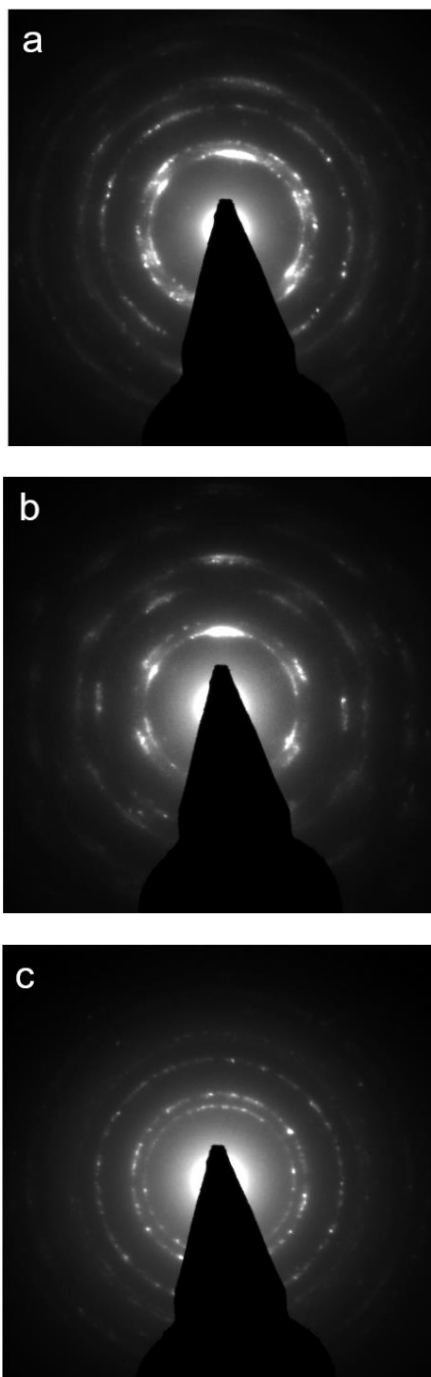
Figure 18. Diffraction pattern images of the Ti films at the electric bias of a) −70V b) 0V and c) +30V.
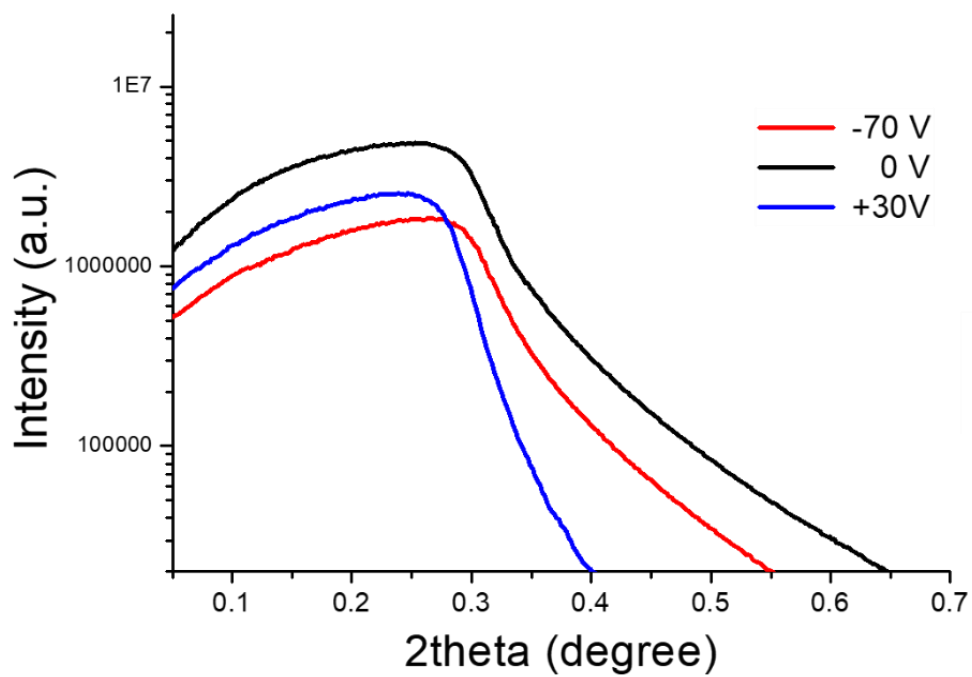
Figure 19. XRR data of the Ti films in the range of 0 ° ~ 0.7 ° at the electric bias of −70V, 0V and +30V.

Substrate bias (V)	−70	0	+30
Thickness (nm)	180	146	92
Critical angle (degree)	0.31	0.28	0.25
Calculated density (g/ cm^3)	4.974	4.058	3.499
Crystallinity	High	High	Low

Table 2. Characteristics of the Ti films with thickness, crystallinity, the calculated density and the measured critical angle by XRR at the electric bias of −70V, 0V and +30V.

Chapter 3.

Preparation of highly (002) oriented Ti films on a floating Si (100) substrate by RF magnetron sputtering

3.1. Introduction

Ti has been used in micro-electro-mechanical system (MEMS) technology, electronic devices, bio-applications, mechanical equipment [43-48]. Especially, the Ti thin film is a strong candidate for bottom layers of piezoelectric aluminum nitride (AlN) electrodes in manufacturing high frequency bulk acoustic wave devices or surface acoustic resonators [75-78]. Many efforts have been made to obtain (002) oriented AlN electrodes, which have an outstanding piezoelectric property and are strongly affected by the orientation and crystallinity of bottom metal layers such as Ti, Pt/ Ti, Al, Mo and Pt. Among them, Ti films were the most desirable for AlN electrodes [77]. Among various Ti orientations, the (002) oriented Ti film was optimum for the (002) growth of AlN [76]. Therefore, the

growth of highly (002) oriented Ti films has been an important issue in sputtering.

Many researchers have widely studied the influences of deposition parameters such as sputtering power, pressure, substrate temperature and the distance between the target and the substrate on properties and microstructure of Ti films using DC sputtering [49-53]. However, a few researchers have tried to deposit Ti films using RF sputtering although RF sputtering has an advantage of a high degree of ionization due to electrons oscillations in the plasma [54, 55].

Meanwhile, there are some methods, which are bias sputtering [79], ion beam assisted deposition (IBAD) [80] and electron cyclotron resonance (ECR) [81], to adjust the incident energy of ions in the plasma since the incident energy of ions into a substrate affects the deposition behavior of a thin film. In these methods, however, the electric bias should be applied to the substrate that could interfere the plasma condition or require an expensive and complicated equipment. Therefore, RF sputtering can be a simple and effective candidate to use the incident energy of ions because it has the high degree of ionization.

In this chapter, RF sputtering is used to prepare (002) oriented Ti films. In our preliminary experiment, it was

observed that the different microstructure of Ti films was evolved between floating and grounded substrates. Therefore, we focused on comparing the deposition behavior between floating and grounded substrates. The highly (002) oriented Ti films were deposited on the floating Si (100) substrate whereas Ti films of various orientations were deposited on the grounded one. The different deposition behavior between floating and grounded substrates was approached by comparing the incident energy of ions between floating and grounded substrates during RF sputtering. The deposited films were analyzed by FESEM, XRD and TEM.

3.2. Experimental methods

The cylindrical sputtering chamber made of stainless steel was 30 cm in diameter and 18 cm in length. The Ti target of 10 cm in diameter was used. The distance between the target and the substrate was 6 cm. The plasma was generated by a RF power supply and a matching network (13.56 MHz). The base pressure was ~5 × 10^{-6} Torr. The substrate for deposition of Ti films was a Si (100) wafer of 2 cm × 4 cm, which was cleaned by a buffered oxide etchant (BOE) and washed by deionized water to remove a native oxide layer.

To compare the deposition behavior between floating and grounded substrates, Ti films were simultaneously deposited on floating and grounded substrates with varying Ar (99.999%) pressures of 5 ~ 30 mTorr and a RF power of 160 W, which corresponds to 2 W/ cm^2 for the target. To float the substrate electrically, a thin alumina sheet of 5 mm × 10 mm × 1 mm was placed between the substrate and the grounded stainless holder.

Crystallinity of the films deposited on floating and grounded substrates was investigated using high resolution XRD (X'pert Pro, PANalytical) at a 2θ scanning range of 20 ~ 65˚ with the Cu Kα (λ = 1.5418 Å) source. The microstructure of the films was analyzed by FESEM (SUPRA 55VP, Carl Zeiss) and TEM (Tecni F20, FEI).

3.3. Results and Discussion

Ti thin films were deposited on floating and ground substrates with varying Ar gas pressure. Figure 20 shows the FESEM images of Ti films deposited on the floating Si (100) substrate. Figure 20(a)－(f) show the surface morphology of Ti films deposited for 30 min respectively at 5, 10, 15, 20, 25 and 30 mTorr. Well－developed crystalline facets are observed in Figure 20(b), (c) and (d). The grain size decreased abruptly in

Figure 20(e) and (f). Thicknesses of the Ti films, determined by the cross−section FESEM images, which are not shown here, were 378, 524, 463, 417, 245 and 120 nm respectively at 5, 10, 15, 20, 25 and 30 mTorr.

Figure 21 shows the FESEM images of Ti films deposited on the grounded Si (100) substrate. Figure 21(a)−(f) show the surface morphology of Ti films deposited for 30 min respectively at 5, 10, 15, 20, 25 and 30 mTorr. Crystalline facets in Figure 21(b), (c) and (d) were less developed than those in Figure 20(b), (c) and (d), indicating that making the substrate electrically floating has an effect on the crystalline quality. As in Figure 20(e) and (f), the grain size decreased abruptly in Figure 21(e) and (f). Thicknesses of the Ti films, determined by the cross−section FESEM images, were 422, 516, 400, 421, 229 and 164 nm respectively at 5, 10, 15, 20, 25 and 30 mTorr.

To examine the film crystallinity and any preferred orientation, the films were analyzed by high resolution XRD. Figure 22 shows XRD data of the Ti films grown on floating and grounded substrates at different gas pressure. In Figure 22(a), the Ti films grown on the floating Si (100) substrate at 5 ~ 30 mTorr showed the dominant XRD peak at $2\theta = 38°$ which represents (002) orientation. It is noted that a nearly single

peak of (002) was obtained at 20 mTorr. It appears that the facet development in Fig. 1 corresponds to the XRD peak of (002) in Figure 22(a). For example, the well-developed facet in Figure 20(d) appears to match with the highest peak intensity of (002) in Fig. 3(a). In the films of Figure 20(e) and (f), which had the abruptly decreased grain size, the (002) peak was negligible in Figure 22(a).

In Figure 22(b), the Ti films grown on the grounded Si (100) substrate at 5 ~ 30 mTorr showed the XRD peaks at $2\theta = 35°$, 38°, and 40° which represent the (100), (002), and (101) orientation, respectively. The (002) orientation was dominant at 5 ~ 20 mTorr and the (101) orientation appeared when the gas pressure decreased to 5 and 10 mTorr. On the other hand, the (100) orientation was dominant at 25 and 30 mTorr. As the FESEM images of the films deposited on the floating substrate in Figure 20 were related with the XRD data in Figure 22(a), the FESEM images of the films on the grounded substrate in Figure 21 were also related with the XRD data in Figure 22(b). For example, the large grain size in Figure 20(c) and (d) appears to match with the high intensity of (002) in Figure 22(b) at 15 and 20 mTorr. In the films of Figure 21(e) and (f), which had the abruptly decreased grain size, the (002) peak was negligible in Figure 22(b).

It is noted that the preferred orientation of Ti films was quite different between floating and grounded substrates. The highly (002) oriented Ti films grew dominantly on the floating substrate with a negligible (100) peak whereas the (100) and (002) oriented Ti films grew on the grounded substrate. At 25 and 30 mTorr, where the (002) peak disappeared, the (100) peak became dominant in the films on the grounded substrate.

Using the full width at half maximum (FWHM), the (002) peak in Figure 22 can be analyzed more quantitatively. Figure 23 shows the FWHM and the grain size calculated by the Scherrer equation [82] corresponding to the (002) peak of Ti films grown on floating and ground substrates at different gas pressure. In case of the floating substrate, the FWHM and grain size at 20 mTorr were respectively 0.42 and 20.9 nm, which were the same as those at 15 mTorr. These values of FWHM and the grain size were respectively the smallest and the largest in Figure 22(a). In case of the grounded substrate, the smallest FWHM and the largest grain size, which were obtained at 15 mTorr, were respectively 0.425 and 20.7 nm as shown in Figure 22(b).

To investigate the preferred growth of the (002) orientation of Ti films further, the XRD peak intensity ratio of (100) to (002) was plotted in Figure 24. The lowest XRD peak

intensity ratio of (100) to (002), which can be used as a measure for the preferred (002) orientation, was exhibited at 10 and 20 mTorr for the floating substrate and at 15 mTorr for the grounded substrate. Moreover, in Figure 22, the Ti film deposited at 20 mTorr on the floating substrate had the strongest (002) peak. Therefore, the Ti film on the floating substrate at 20 mTorr was considered to have the highest preferred (002) orientation. To confirm this, the cross-section image of the film deposited at 20 mTorr was analyzed by TEM.

Figure 25(a) shows the high resolution TEM image of the Ti film deposited at 20 mTorr on the floating Si (100) substrate. The lattice image of the Ti film indicated the polycrystalline nature. In order to determine the direction of c-axis of the Si substrate, the diffraction pattern was obtained from the box 'b' in the right bottom of Figure 25(a) and shown in Figure 25(b).The diffraction peak marked by the circle in Figure 25(b) represented the lattice spacing of Si (002). In order to determine the orientation of the Ti film, the diffraction pattern was obtained from the box 'c' in the right bottom of Figure 25(a) and shown in Figure 25(c). The diffraction peak in the circle in Figure 25(c) represented not only the lattice spacing of Si (002) but also the lattice spacing of Ti (002). The inset of the magnified circle in Figure 25(c) revealed that the (002)

orientation of Ti film indicated by the upper arrow grew along the c–axis of the Si substrate indicated by the lower arrow.

Since the observation by high resolution TEM is limited to an extremely local area near the interface, it was not sure whether the preferred growth of Ti (002) along the c–axis of Si was applicable to the more extended region of the film. In order to examine the preferred growth of Ti (002) in the more extended region, a dark–field TEM image of the selected diffraction pattern corresponding to the Ti (002) orientation was observed as shown in Figure 26(a), where the selected Ti (002) orientation was indicated by the upper arrow in the diffraction pattern in the inset.

In the dark–field TEM image of Figure 26(a), the area corresponding to the selected Ti (002) orientation appeared selectively bright, indicating that Ti (002) was developed in the more extended area. Figure 26(b) shows a bright–field TEM image of Figure 26(a). If Figure 26(a) and (b) are compared, it is seen that the (002) oriented Ti film grew from the interface with the Si substrate to the end of the Ti film.

Then, we need to think about why the Ti films on the floating substrate had higher tendency of (002) preferred growth than those on the grounded substrate. One possibility for the difference in the deposition behavior between floating

and grounded substrates would be the incident energy of ions into the substrate. As to the effect of the incident energy, Hoshi et al. [83] reported that the crystal orientation of Ti films with a hcp structure changed from (001) orientation to (100) orientation as the incident energy of the sputtered Ti species increased. Therefore, it is worth to compare the incident energy of ions between floating and grounded substrates.

Kersten et al. [84] suggested that the incident energy of ions could be determined from the substrate temperature. In order to determine the incident energy based on their suggestion, we measured each temperature of floating and grounded substrates by a K−type thermocouple. The measured temperature was used to calculate the energy influx into floating and grounded substrates by the following equations (3.1) ~ (3.3).

$$Q_{net} = \frac{d}{dt}(mcT_{sub}) = mc\frac{d}{dt}T_{sub} \qquad (3.1)$$

$$Q_{net,heating} = Q_{in} + Q_{out} \qquad (3.2)$$

$$Q_{net,cooling} = Q_{out} \qquad (3.3)$$

The net energy flux incident into the substrate can be described by Eq. (3.1), where Q_{net} is the energy flux into (influx) and out of (outflux) the substrate, m is the mass of the

substrate and c is the specific heat capacity.

Q_{net} can be calculated by measuring the rate of change of the substrate temperature, assuming that the mass and the specific heat capacity of the substrate are kept constant. Herein, depending on whether the plasma is turned on (heating) or turned off (cooling), Q_{net} is expressed by Eq. (3.2) or Eq. (3.3). In Eq. (3.3), there is no energy influx because plasma was turned off. Assuming that the energy outflux remains the same immediately before and after the plasma is turned off, the energy influx into the substrate is the difference between Eq. (3.2) and Eq. (3.3) or $Q_{net,heating} - Q_{net,cooling}$. Therefore, the energy influx could be determined using $Q_{net,heating}$ and $Q_{net,cooling}$ calculated by Eq. (3.1).

Figure 27 shows each temperature of floating and ground substrates measured for 120 sec during heating and cooling. Each temperature was measured for 60 sec after the power was turned on and for another 60 sec after the power was turned off. The rate of change of the substrate temperature was estimated using the tangent at 60 sec when the plasma was turned off.

Table 3 shows the rate of change of the substrate temperature and the calculated energy influx into floating and grounded substrates. The energy influxes into floating and

71

grounded substrates were 5.217 and 6.624 mW/ cm^2, respectively. Therefore, the energy influx into the floating substrate was about 20% smaller than that into the grounded substrate.

This difference comes from the fact that the potential difference between the plasma and the floating substrate is different from that between the plasma and the grounded substrate. Plasma and floating potentials are designated respectively as V_P and V_F. V_P is always positive with respect to floating and grounded substrates. Depending on whether V_F is positive or negative, the potential difference $(V_P - V_F)$ between the plasma and the floating substrate becomes smaller or larger than the potential difference $(V_P - 0)$ between the plasma and the grounded substrate.

V_F was measured by a Langmuir probe to be positive under our experiment condition. Thus, the floating substrate has a smaller potential difference than the grounded one. As a result, the floating substrate has the smaller incident energy of ions and thereby a smaller total energy influx.

3.4. Conclusion

Ti films grown on the floating substrate showed the preferred (002) orientation, whereas those grown on the grounded substrate showed (002), (100) and (101) orientations. Such a difference could be explained by the calculation of the energy influx, which showed that the floating substrate had the lower energy influx than the grounded substrate. A new RF sputtering method, which simply uses a floating substrate, was developed to prepare the highly (002) oriented Ti thin film, which can be applied for the bottom metal layer of AlN electrodes for piezoelectric devices such as high frequency bulk acoustic wave devices and surface acoustic resonators.
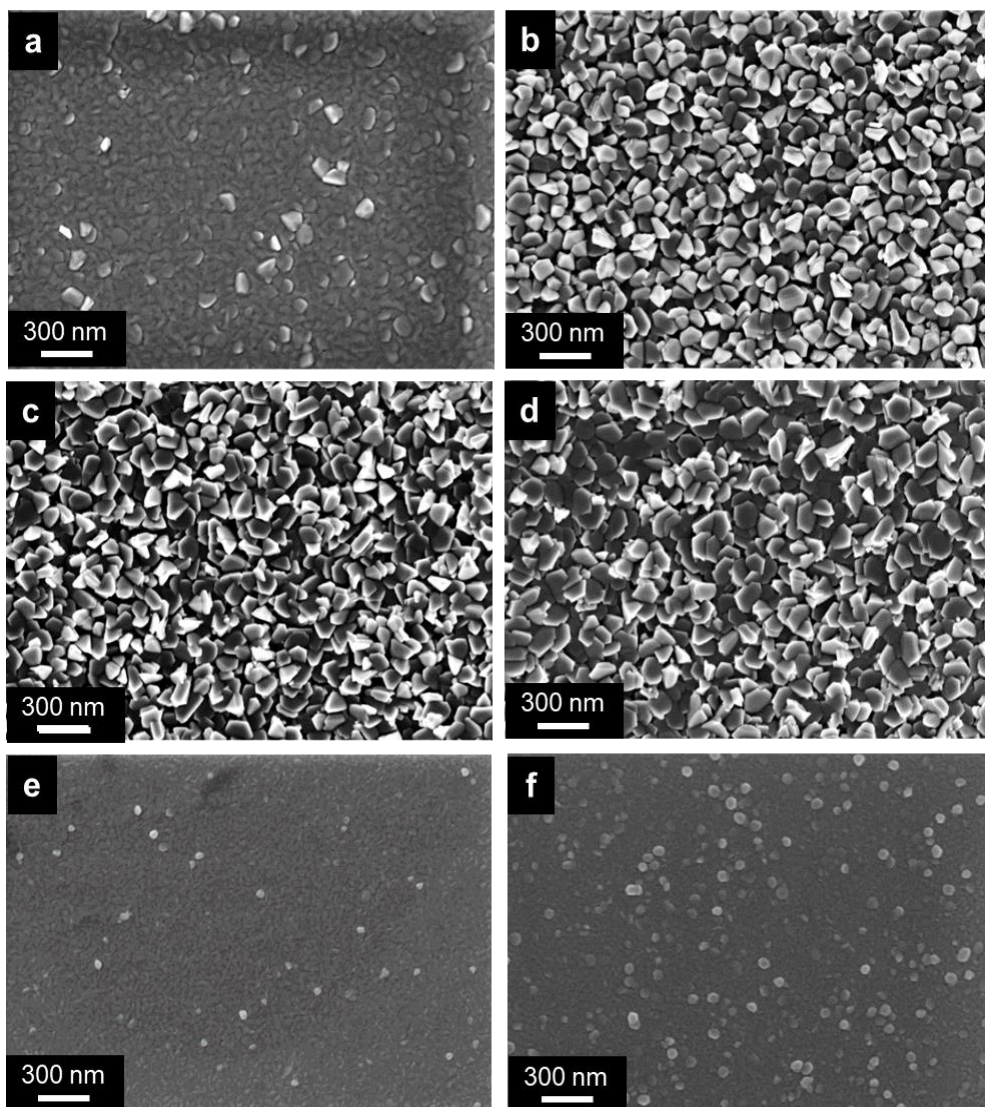
Figure 20. Top-view FESEM images of Ti films deposited on a floating substrate at (a) 5 mTorr (b) 10 mTorr (c) 15 mTorr (d) 20 mTorr (e) 25 mTorr and (f) 30 mTorr.
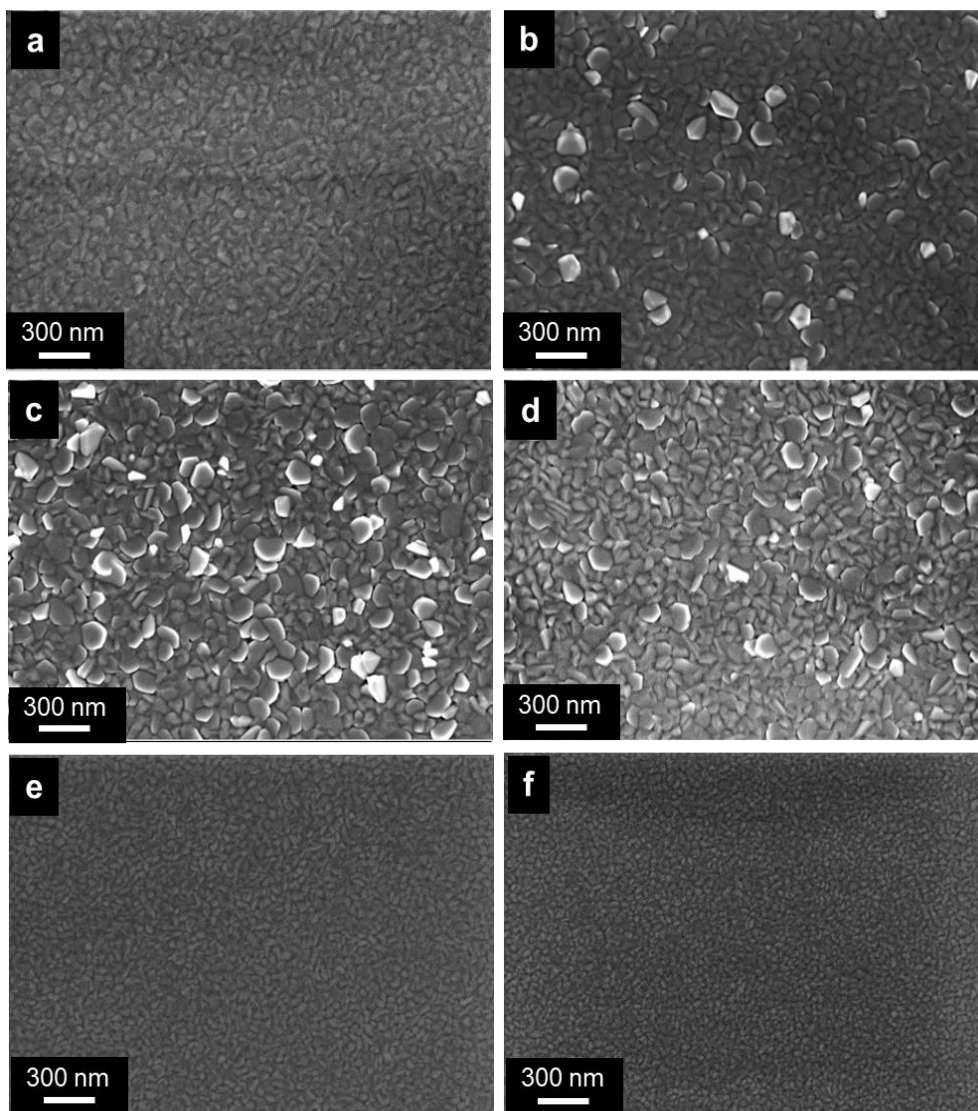
Figure 21. Top-view FESEM images of Ti films deposited on a grounded substrate at (a) 5 mTorr (b) 10 mTorr (c) 15 mTorr (d) 20 mTorr (e) 25 mTorr and (f) 30 mTorr.
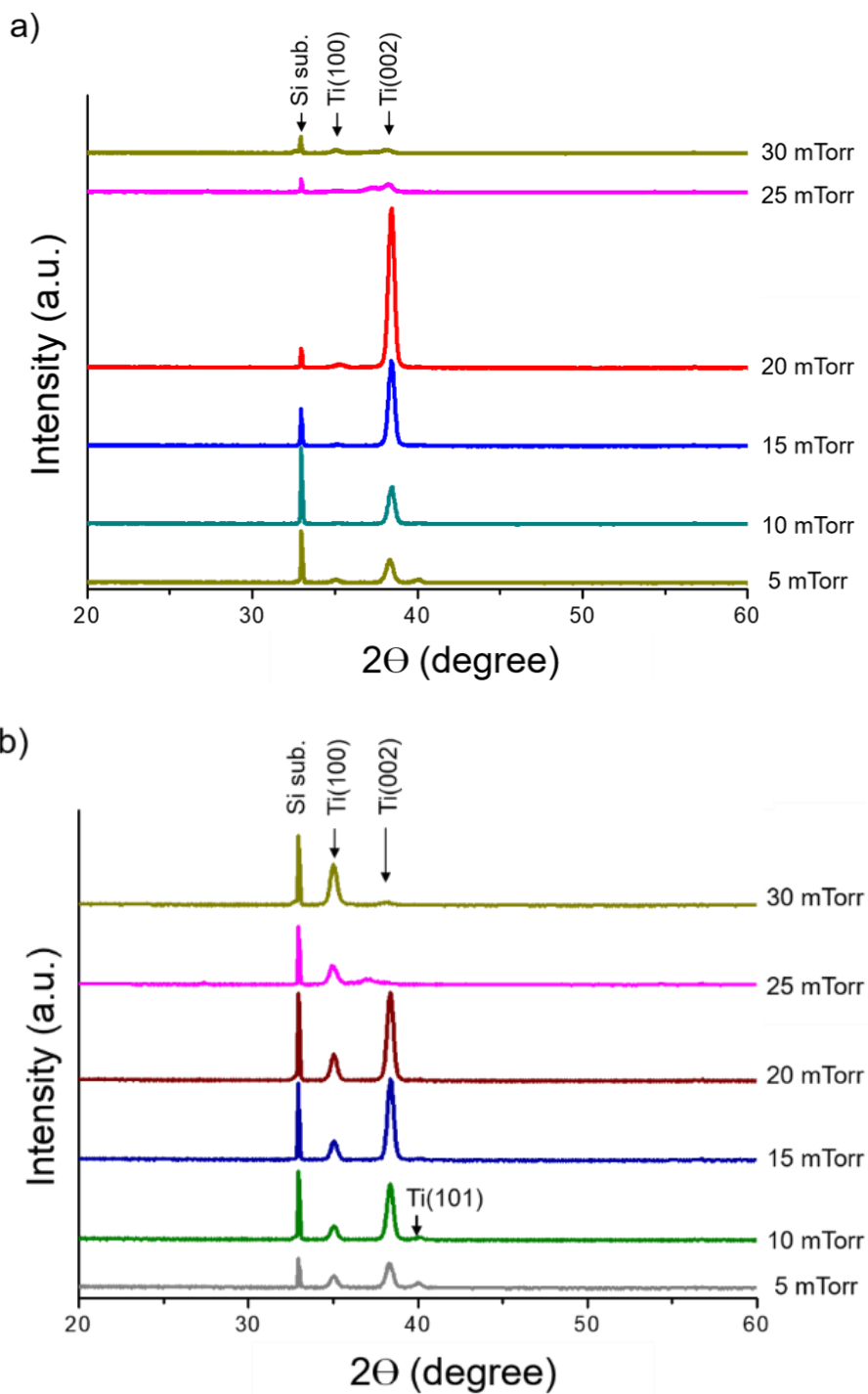
Figure 22. XRD data of Ti films deposited on (a) a floating substrate and (b) a grounded substrate in 2θ range of 20 ~ 60°.
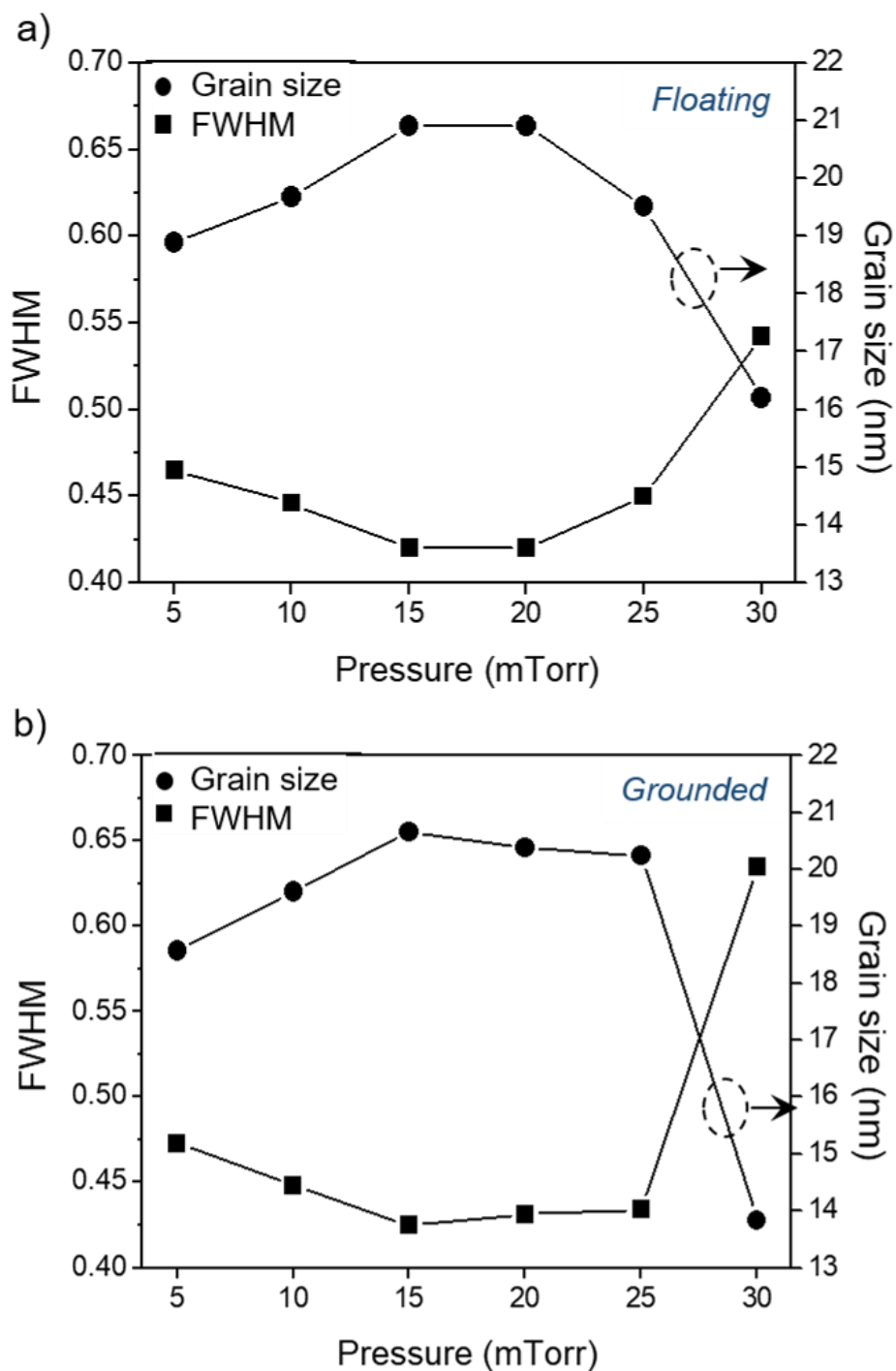
Figure 23. Grain size claculated by Scherrer equation and FWHM of (002) peak from the XRD data of (a) floating and (b) grounded substrates.
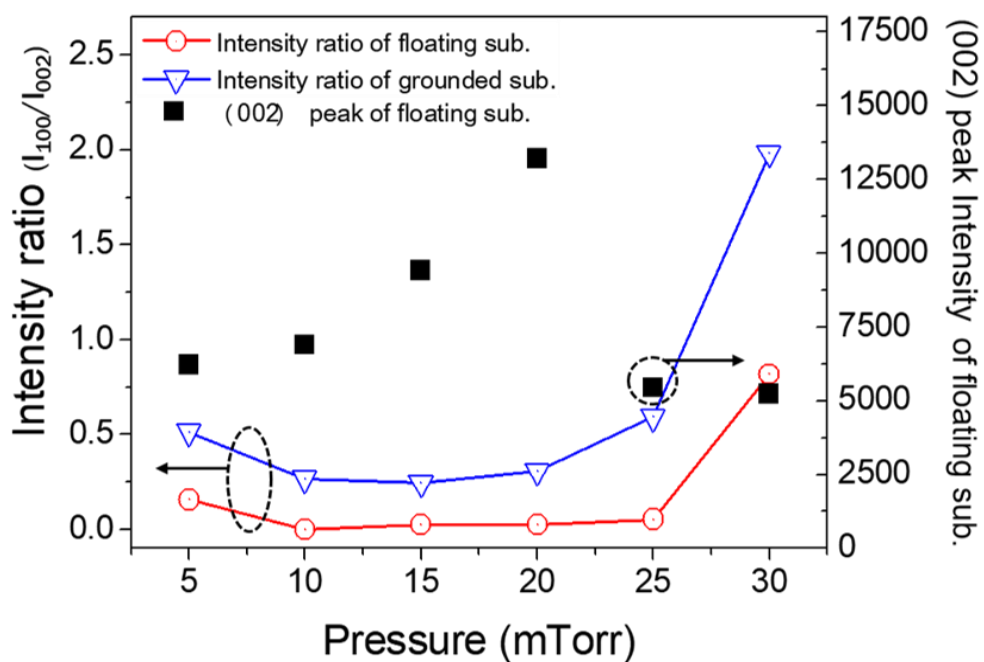
Figure 24. Intensity ratio of (100) to (002) peak from the XRD data of a floating substrate (open inverted triangle) and a grounded substrate (open circle) and the (002) peak intensity of a floating substrate (closed square).
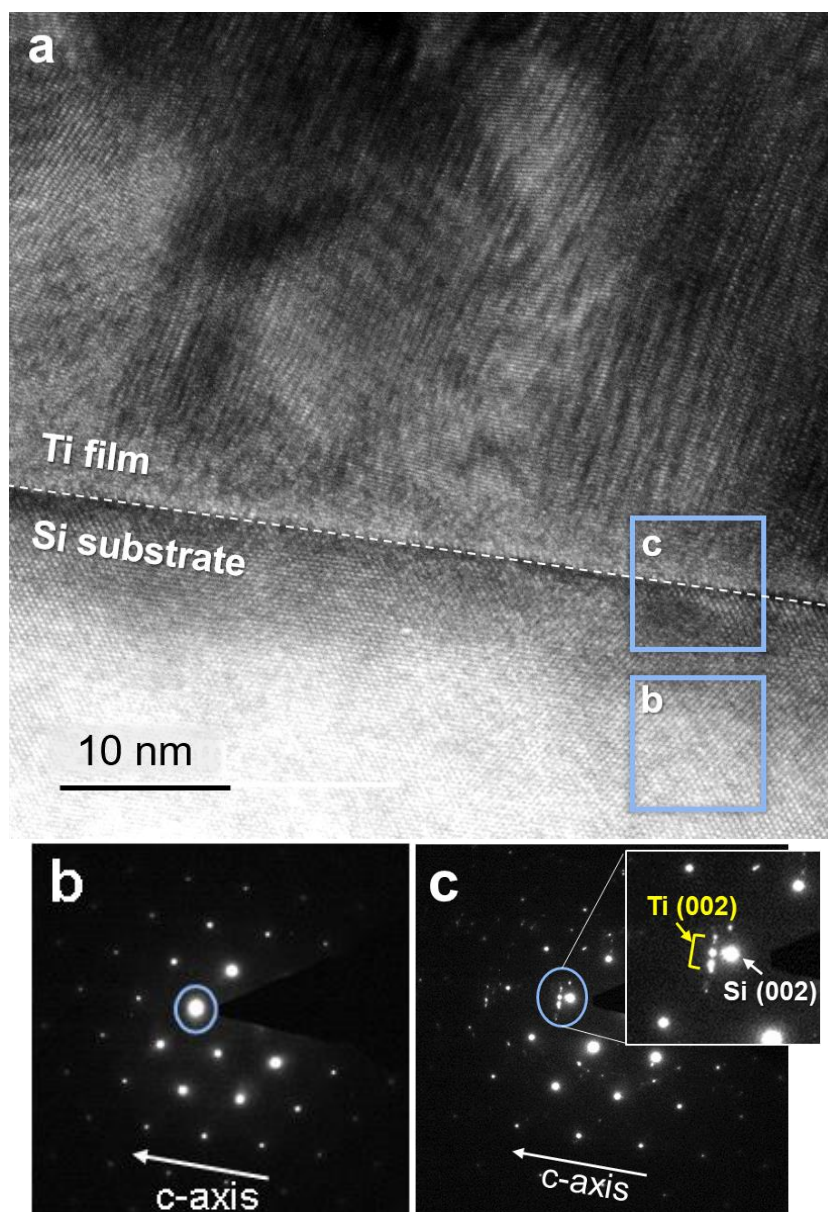
Figure 25. (a) Cross−section high resolution TEM image of Ti film on a floating substrate at 20 mTorr and diffraction pattern images of (b) the Si substrate and (c) the interface between the substrate and Ti film and the diffraction patterns as marked by the arrows in the inset of (c) denote the information of Si (100) substrate and the (002) orientation of Ti film.
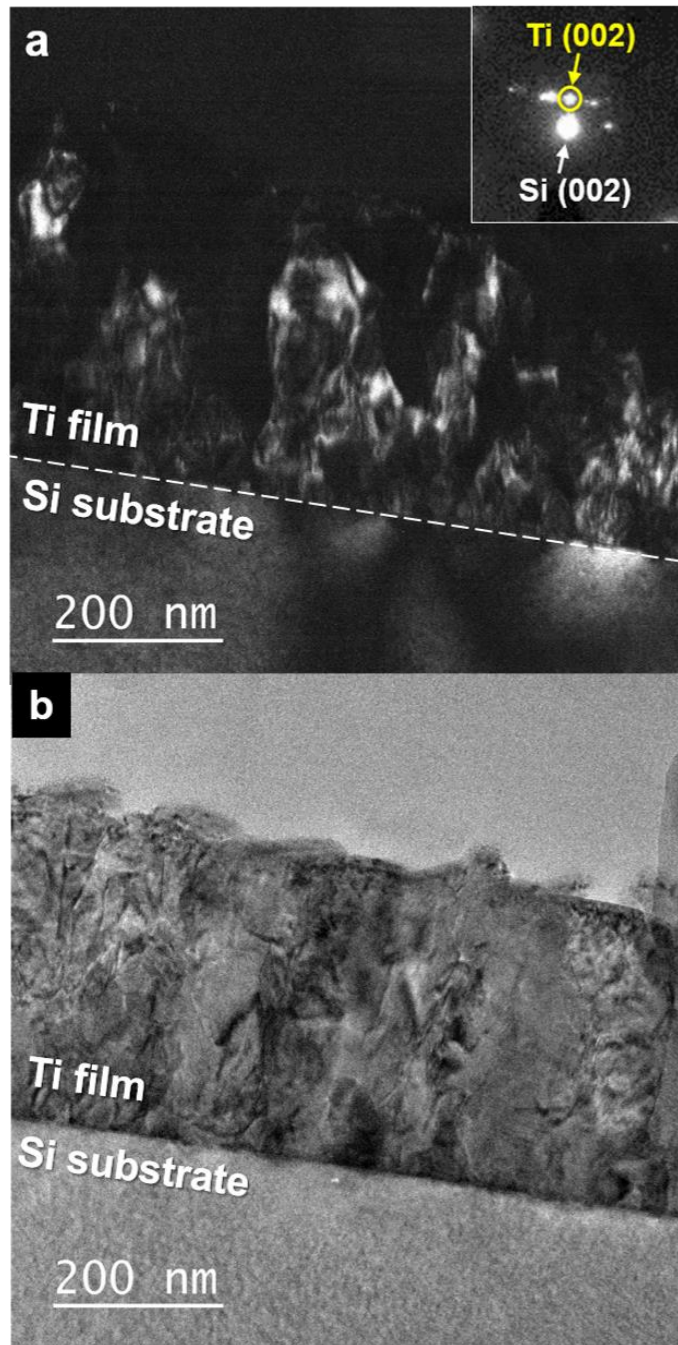
Figure 26. (a) Dark-field TEM image of a selected Ti (002) diffraction pattern as marked by the arrow in the upper right inset and (b) bright-field TEM image of the image (a).
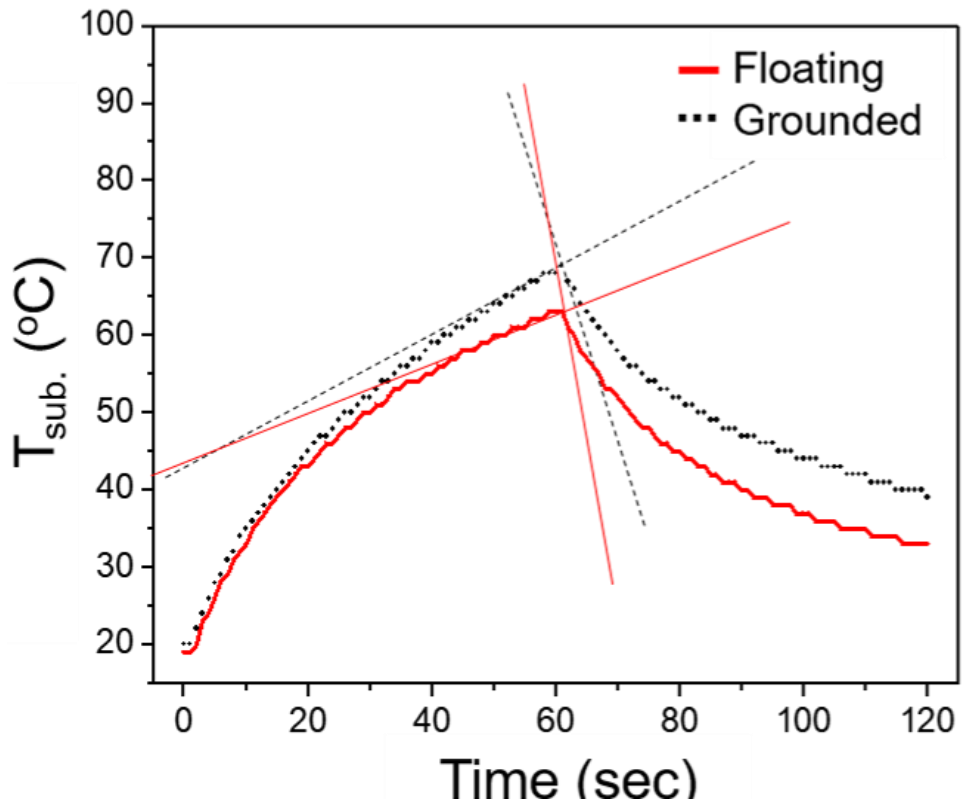
Figure 27. Measurements of floating and grounded substrate temperatures during 60 sec of plasma on and another 60 sec of plasma off for estimating the energy influx.

	$\dfrac{d}{dt}T_{heating}$	$\dfrac{d}{dt}T_{cooling}$	$Q_{in}\left[mW/cm^2\right]$
Grounded sub.	1.844	-2	6.624
Floating sub.	1.059	-2	5.271

Table 3 Summary of the rate of change of floating and grounded substrate temperatures and estimated energy influx of each substrate

Chapter 4.

In-situ plasma diagnostics for investigating charged species during Ti RF magnetron sputtering

4.1. Introduction

Generation of charged nanoparticles and their effects on a film deposition is experimentally confirmed during RF magnetron sputtering. Meanwhile, it is also necessary to conduct in－situ plasma diagnostics during the process for investigating the consistent plasma condition and further information of the plasma. When the same plasma condition is remained, the consistent and reliable experiment results can be obtained. However, the plasma condition could be sensitive to small changes and affect the entire process and results. Also, various plasma diagnostics technique can broadly provide the information of the plasma condition such as electron and ion temperature, plasma density, species compositions and ion energy distribution.

Therefore, in－situ plasma diagnostics were conducted by optical emission spectroscopy (OES) and ion mass analyzer. OES can discriminate the type of ions or charged species and their energy status. Ion energy analyzer can investigate energy distribution of ions or charged specie. From these diagnostics, it is possible to in－situ analyze the generation and the behavior of the charged nanoparticles during the process.

A. OES diagnostics

OES is a reliable and extensively used analytical technique used to establish the elemental composition of a wide range of metals. The type of samples which can be analyzed using OES include samples from the melt in primary and secondary metal production, and in the metals processing industries bolts, tubes, wires, rods, plates and so on. OES uses the part of the electromagnetic spectrum including the visible spectrum and part of the ultraviolet spectrum. That's from 130 nm up to around 800 nm, in terms of wavelength. And OES is capable of analyzing a wide range of elements from Lithium to Uranium in solid metal examples covering an extensive concentration range, providing low detection limits, high precision, and very high accuracy. The elements and concentrations that can be determined by OES analyzers depend on the material being

tested and the type of analyzer used.

When an atom interacts with the energy of an electrical discharge, some of the electrons in the outer shells of the atom are ejected. Since outer-shell electrons are further away from the nucleus, they are less tightly bound to the nucleus of the atom and hence require less input energy. The ejected electrons make the atom unstable by creating a vacancy. In order to restore stability, electrons from higher orbits which are further away from the nucleus drop down to fill the vacancy. As the electrons move between the two energy levels or shells, excess energy is released and this is emitted in the form of element-specific light or optical emission.

A series of spectral lines, which correspond to different electron transitions between the different energy levels or shells, is emitted by every element. Each transition generates a particular optical emission line with a fixed wavelength or energy of radiation. For a typical metallic sample containing manganese, iron, nickel, chromium, vanadium, etc., each element emits many wavelengths, resulting in a line-rich spectrum. For instance, iron emits just over 8000 different wavelengths, which means it is important to select the optimum emission line for a given element in a sample. The atoms emit the characteristic light, which is transmitted to the optical

system where it gets separated into its spectral wavelengths by the high－tech grading containing up to 3600 grooves per millimeter [85]

B. Ion energy analyzer

Ion energy analyzer are used to measure the distribution of energy incident on the substrate. The method of measuring the energy distribution of incident ions is composed of three grids, including a retarding grid, and a Faraday cup for collecting ions as shown in Figure 28 []. The ion energy distribution through the I－V curve of the ion energy analyzer can be obtained by differentiating the I－V curve according to the voltage as shown in Figure 29 [86].

4.2. Experimental methods

Plasma diagnostics were conducted under the same condition with the experiment as mentioned in the chapter 2 and 3.

A. OES diagnostics

The base pressure was ~5 × 10^{-6} Torr. The process pressures and a RF power were respectively 5 ~ 30 mTorr and

160 W, which corresponds to 2 W/ cm^2 for the target.

The relevant emission intensities of plasma species at the substrate position were characterized by OES in the wavelength range of 300 ~ 1000 nm. The OES spectral data were acquired through an optical fiber using the Acton Spectra Pro 500i spectrometer with a resolution of 0.05 nm, a 10 μm broad entrance slit, and a grating of 1200 grooves/ mm. The equipment was combined with a PIMAX CCD camera (from Princeton instrument) and a computer. The software for the spectral acquisition is WinSpec32TM.

B. Ion energy analyzer

The process condition for ion energy analyzer diagnostics is the same as that for OES diagnostics, except that process pressure were 20 mTorr.

And we installed the composition of three grid and digital multimeter (DMM) as shown in Figure 30. In Figure 31(a), Of parts of the three grids, the first grid, marked by grounded mesh, prevents the plasma from clogging in front of the ion energy analyzer so that it is at ground potential just like the surrounding chamber walls. The grid must have an open length of 2 to 3 times the length of the divider to prevent plasma from penetrating into the grid. Therefore, it is necessary to use a

grid with open holes on the order of 100 ~ 200 μm. The second grid, marked by negative bias, is a grid that attract electrons from the plasma into the ion energy analyzer and has a negative potential. The negative voltage of -200V applied should be higher than the energy of the incident electrons to prevent all incoming electrons from entering the grid. In Figure 31(b), the third grid, marked by positive bias, applies a positive variable voltage as a grid to analyze the energy of ions passing through the first and second grids, changing the voltage from a voltage that passes all incoming ions to a voltage that does not pass all or some. The fourth is a substrate as same as a Faraday cup. The ion current passing through the third grid is measured using a DMM connected with the substrate. Secondary electrons may be generated when ions enter the substrate, and the generated secondary electrons may be accelerated by the potential difference between Faraday Cup (in our case, substrate) and the third grid, and thus may be measured as if two ions have reached one ion. Thus, additional grids may be installed, such as a grid with some potential between the third grid and the Faraday cups to prevent the emitted secondary electrons from escaping. However, it was not installed under our experimental conditions.

As measured in the Figure 29, the current characteristics

according to voltage are shown in the following equation.

$$I = 0.5 n_i TA_e \left[\frac{kT_e}{M} \right]^{1/2} \exp \left[\frac{-e(V - V_P)}{kT_i} \right] \quad V \geq V_P \quad (4.1)$$

$$I = 0.5 n_i TA_e \left[\frac{kT_e}{M} \right]^{1/2} \quad V \leq V_P \quad (4.2)$$

Where n_i is the ion density, T is the total transmittance of the grid, A is the open area of the ion energy analyzer, M is the mass of ions, V is the third grid voltage, V_P is the plasma potential, kT_e is the electron temperature, and kT_i is the ion temperature. The second equation is the ion current value that is saturated and measured highest. The ion energy distribution through the I−V curve of the ion energy analyzer can be obtained by differentiating the I−V curve according to the voltage. The differential equation for this is shown below.

$$F(V_o) = \frac{d\left(\frac{I}{I_o} \right)}{dV} \Bigg|_{V=V_o} = \frac{I(V_o) - I(V_o - \Delta V)}{I_o \Delta V} \quad (4.3)$$

4.3. Results and Discussion

A. OES diagnostics

We measure the optical emission at the substrate position to study the emissions from excited species. Figure 32 shows typical OES spectra measured in the wavelength range 300–1000 nm at different process pressure. The leading emission lines in the spectra belong to Ar (750 nm) and Ar^+ (454 nm) emissions. Also, there is a trace of atomic Ti (365.8 nm) and Ti^+ (375.8 nm) at different process pressure. As increasing process pressure, the peak intensity of Ar^+ (454 nm), Ti (365.8 nm) and Ti^+ (375.8 nm) were increased up to 25 mTorr and saturated at 30 mTorr. It is attributed that the more discharging gas (Ar) flow inert into chamber and the more sputtered species come from a target, but Ar gas flow is too high to decease sputtering impact and sputter yield due to collisions of the species in the plasma. Meanwhile, the peak intensity of Ti^+ (375.8 nm) increased in proportion to that of Ti (365.8 nm). It could expected that the ionization of Ti increase proportionally as the amount of sputtered Ti increase. Therefore, we confirmed the sputtered species (Ar, Ar^+, Ti and Ti^+) during the process at different pressure.

B. Ion energy analyzer

I-V curve was successfully measured as shown in Figure 33(a). In Figure 33(b), ion energy distribution was obtained by differentiating the I-V curve of Figure 33(a) according to the voltage. As a result, the energy of positive ions incident into the substrate was measured in the range of 16~17 eV. We expect that positively charged species incident from the plasma, which have the maximum energy of ~17 eV, could be repelled near the substrate when the substrate bias is more than ~17 eV. Considering this result, in chapter 2, we applied to a substrate bias near ~17eV in order to know whether positively charged species are repelled or not, if any. And we confirmed experimentally that the number density of the positively charged Ti NPs captured at a substrate bias of +15V, which is less than 17 eV, was small and decreased considerably. On the other hand, the positively charged Ti NPs captured at a substrate bias of +30V, which is more than 17 eV, was not observed due to being repelled by a substrate bias.

However, it is difficult that the energy distribution different species in the plasma distinguish separately. Since only one peak was obtained, the peak would overlaps with Ar^+ ions and positively charged Ti species as shown in Figure 33(a). As considering ionization rate of sputtered atoms and clusters

during RF sputtering, the peak is expected to be contributed mainly by Ar^+ ions. On the other hand, although it has not been confirmed at all, if there are high energy particles, it would be measured as shown in Figure 34, but it is difficult to measure due to the sensitivity of the current measuring device (DMM) and RF noise.

4.4. Conclusion

Using in-situ plasma diagnostics, we characterized neutral and positively charged species of Ar and Ti in the plasma. Existence and proportion of Ti and Ar species at different process pressure were investigated by OES. Also, the energy distribution of the positively charged species were estimated by ion energy analyzer. Using this result, the energy distribution of positively charged Ti NPs were confirmed experimentally in chapter 2. Therefore, in-situ plasma diagnostics is recommended to understand the plasma process and results correctly.
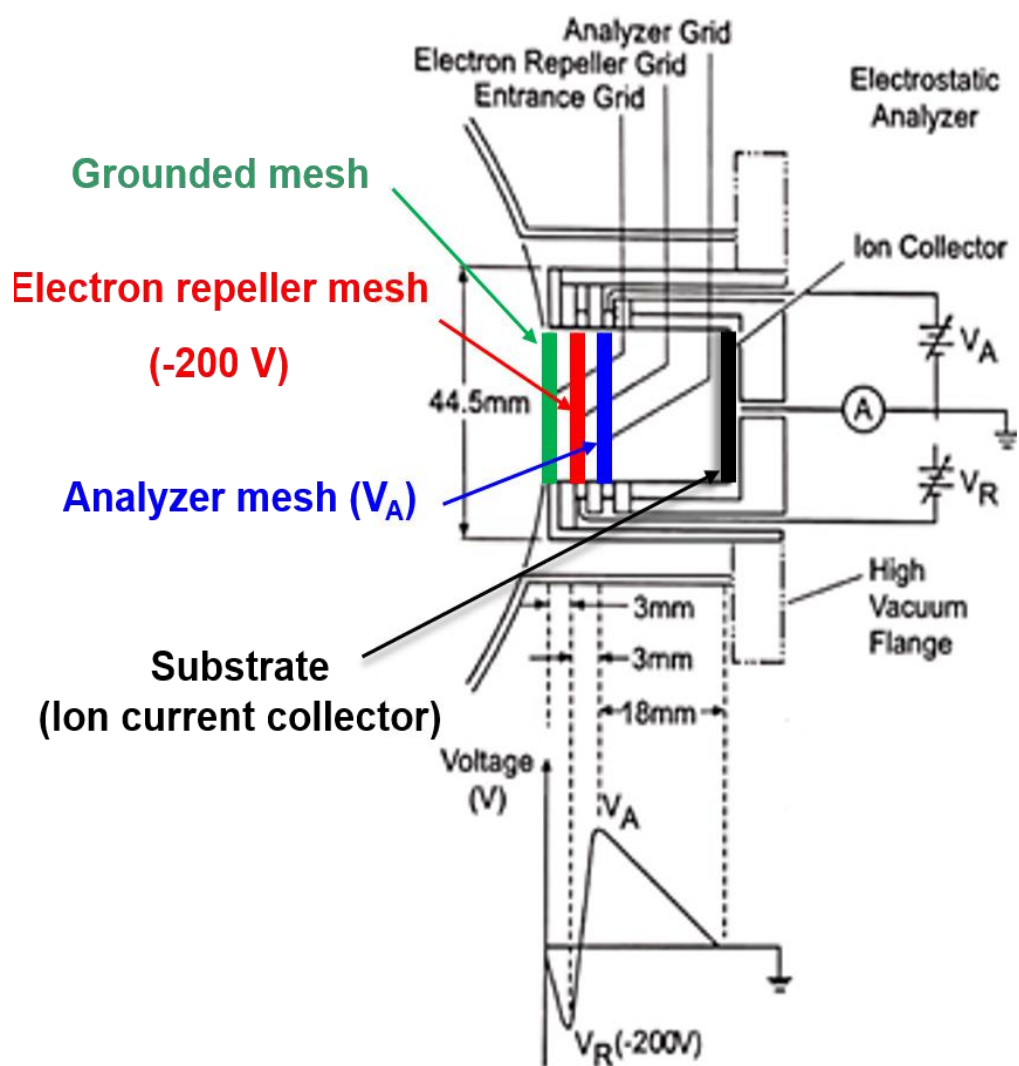
Figure 28. Schematics of ion energy analyzer.
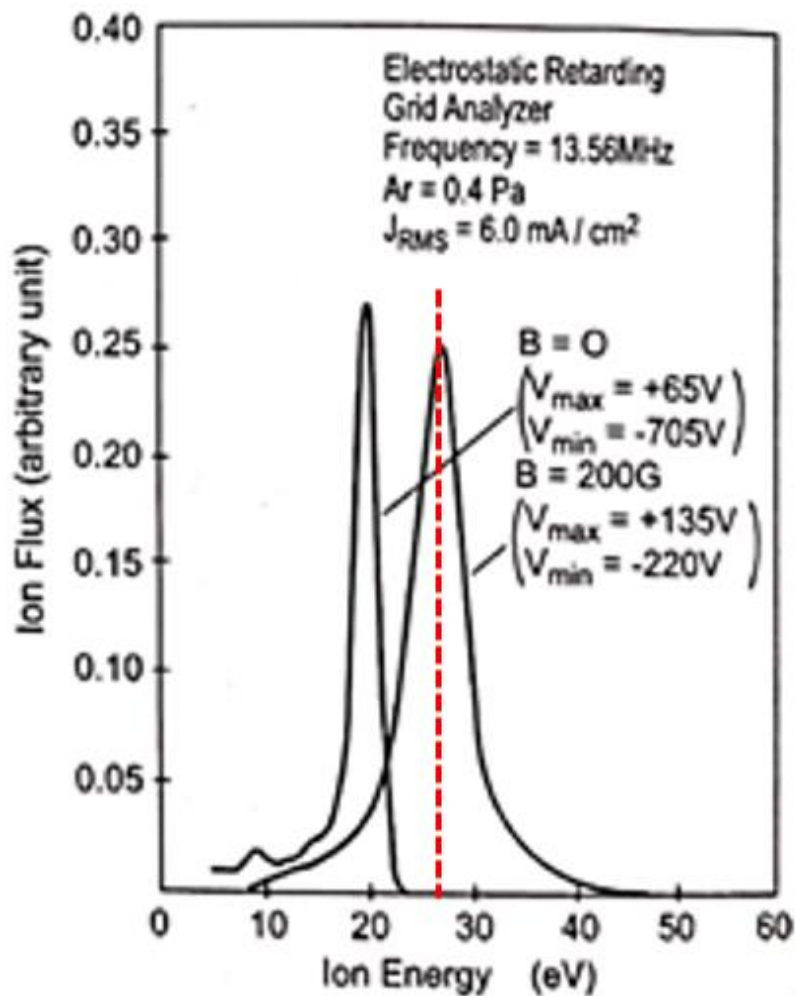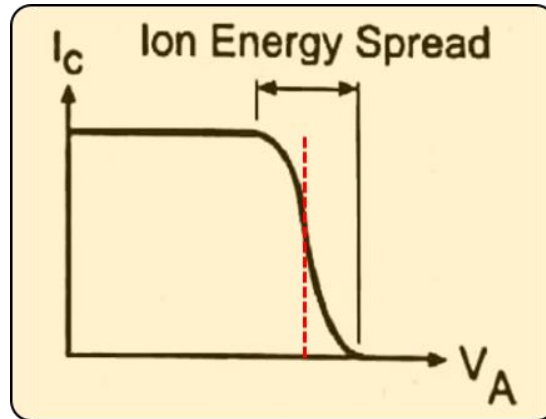
Figure 29. Measurement of I−V curve and calculation of energy distribution.
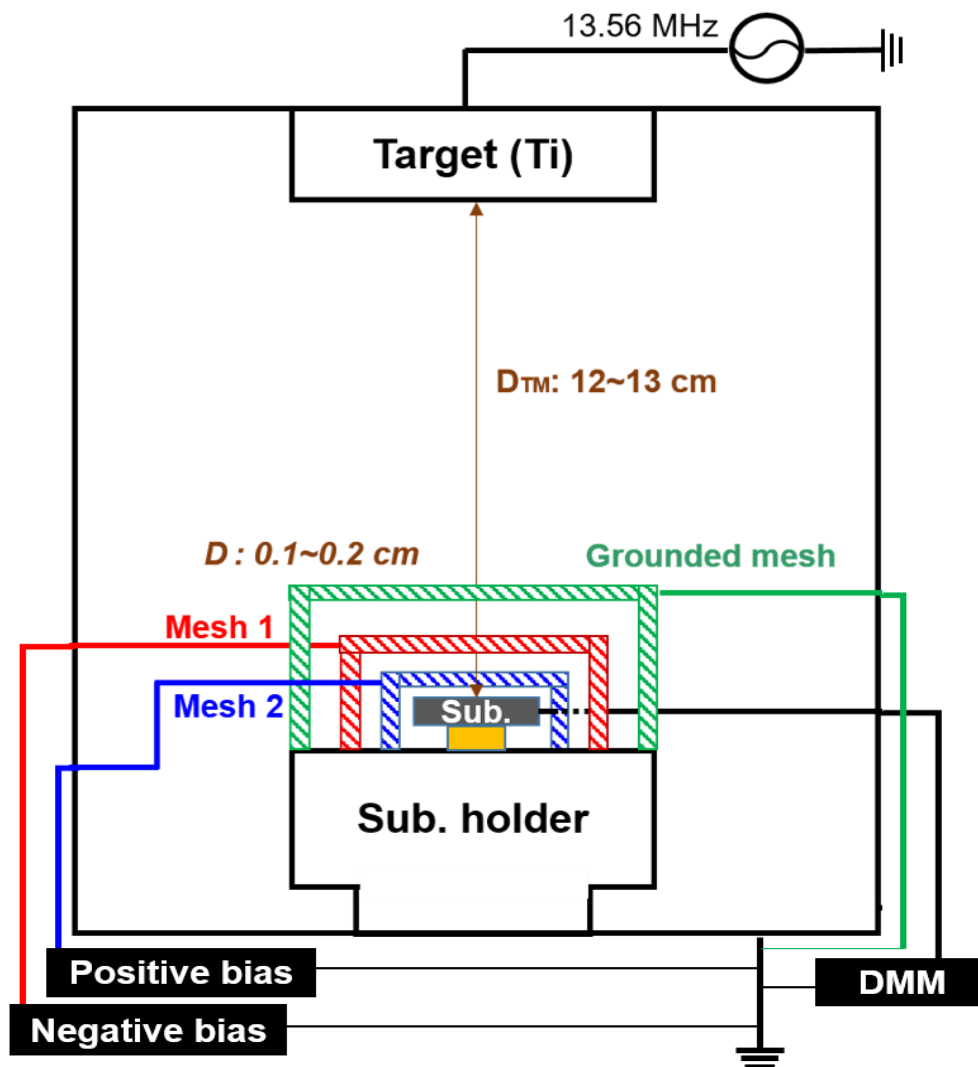
Figure 30. Schematics of installation of ion energy analyzer in RF sputtering chamber.
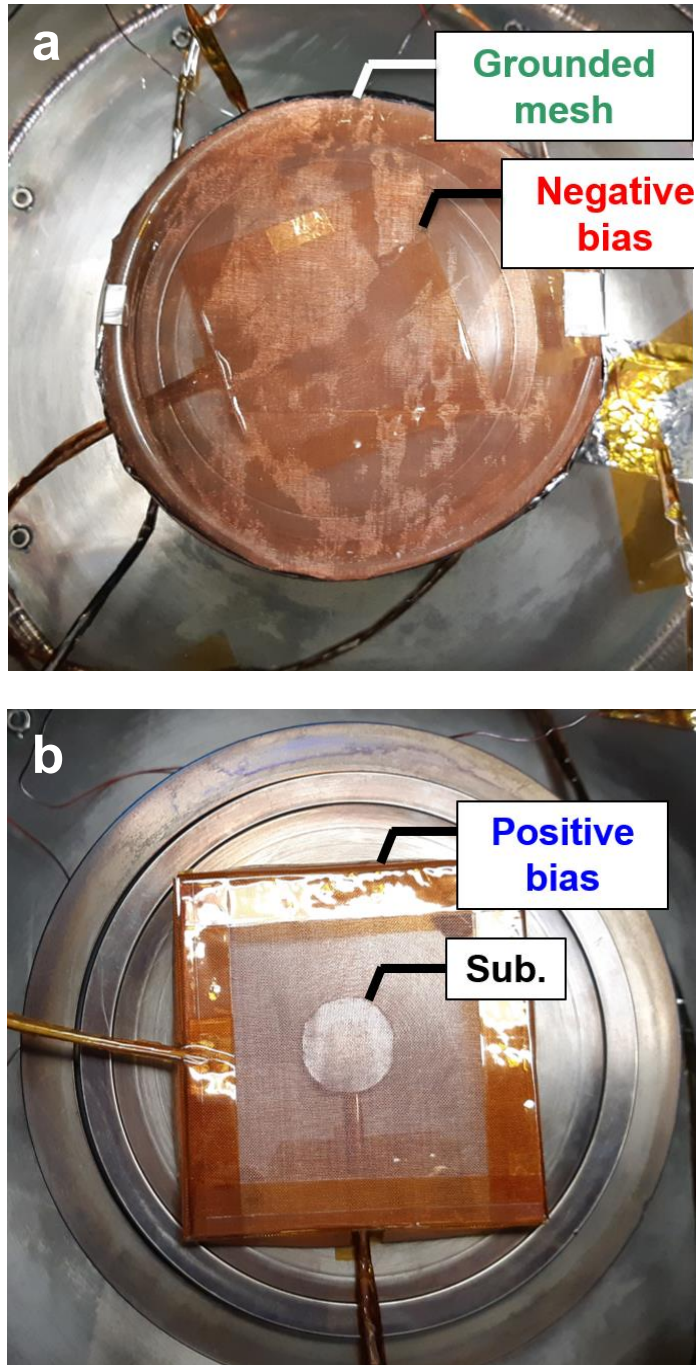
Figure 31. Installed three grids for ion energy analyzer. (a) The first grid and the second grid (b) the third gird and substrate for collecting ion current.
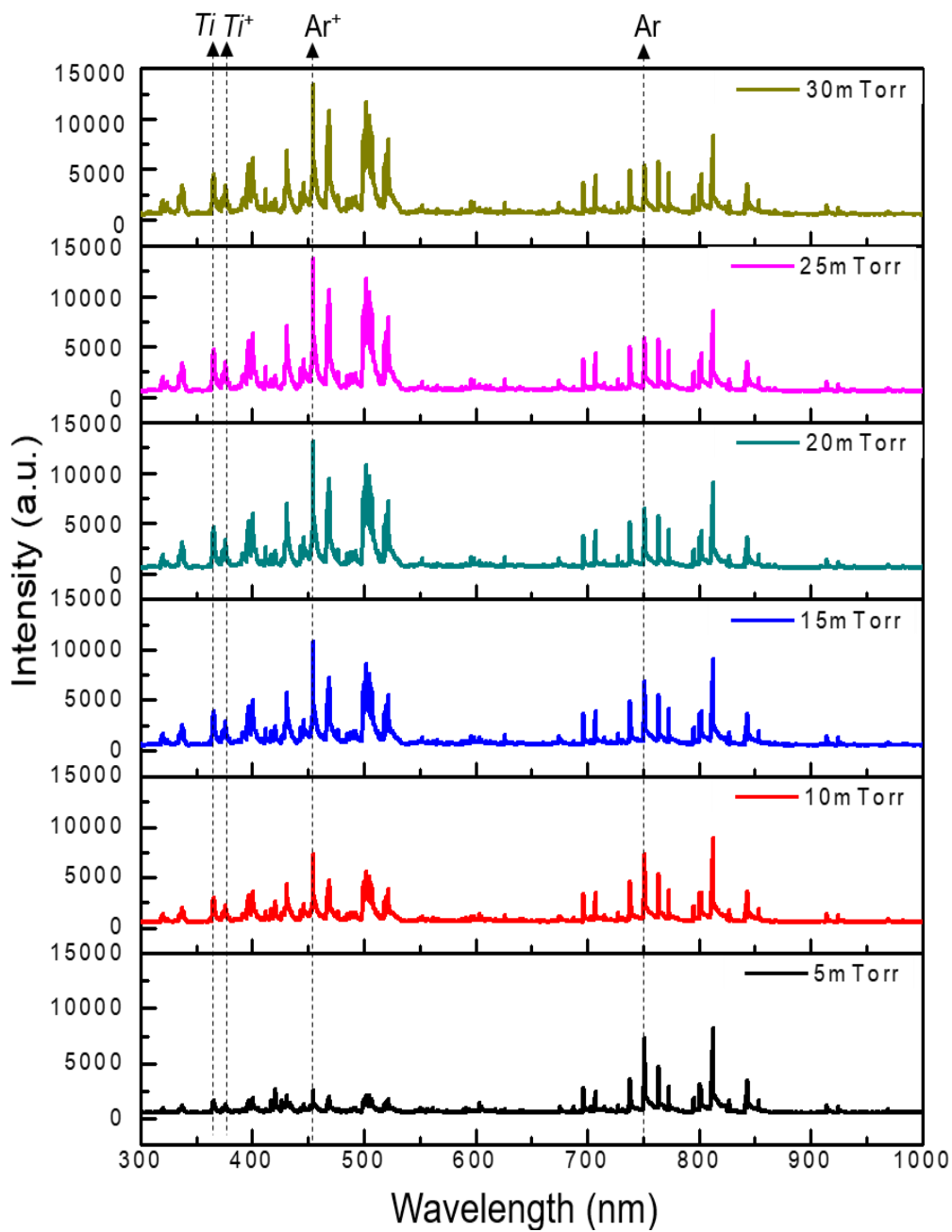
Figure 32. OES measurement at the different gas pressure during Ti RF magnetron sputtering.

97
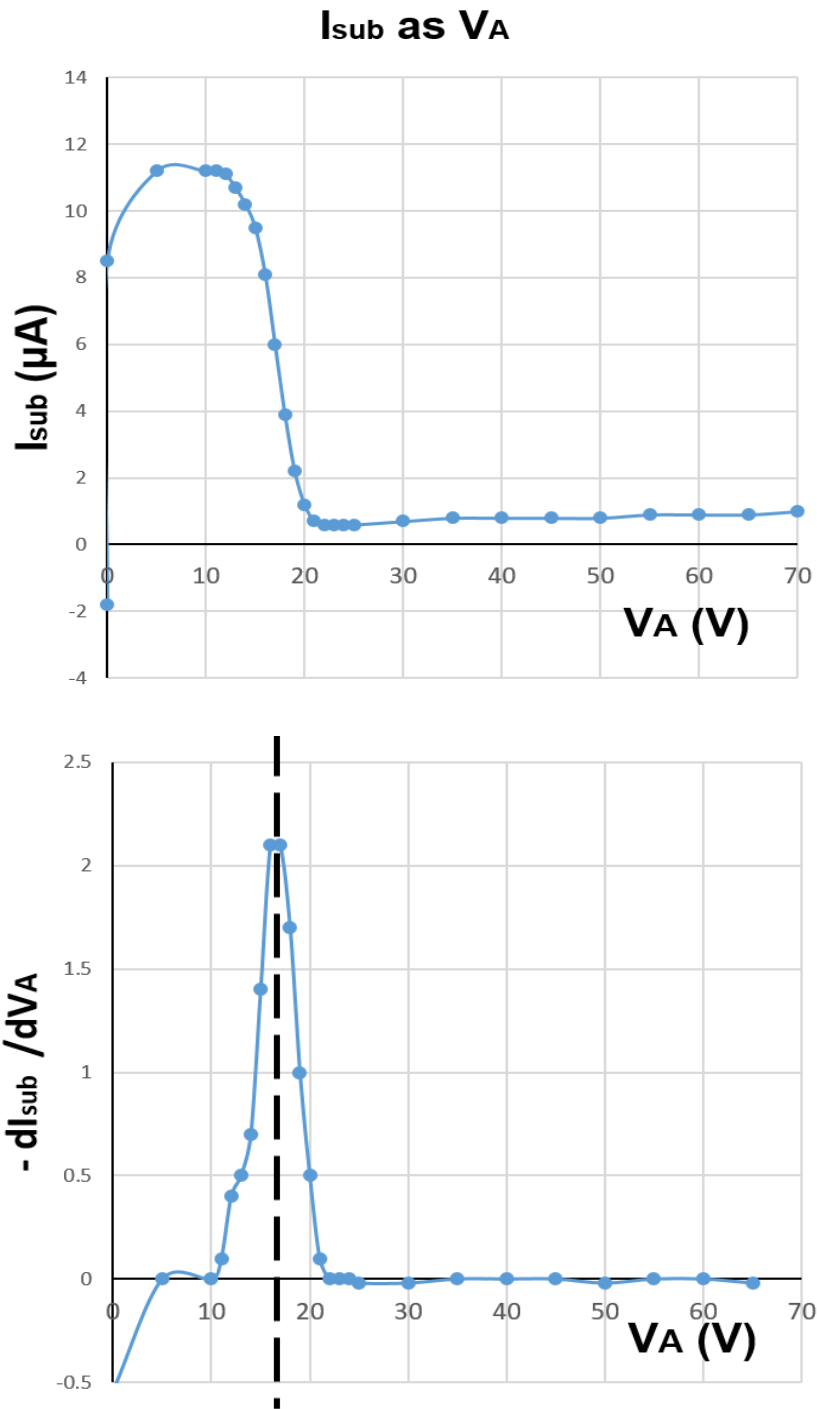
Figure 33. I−V curve measured by ion energy analyzer and calculated energy distribution.
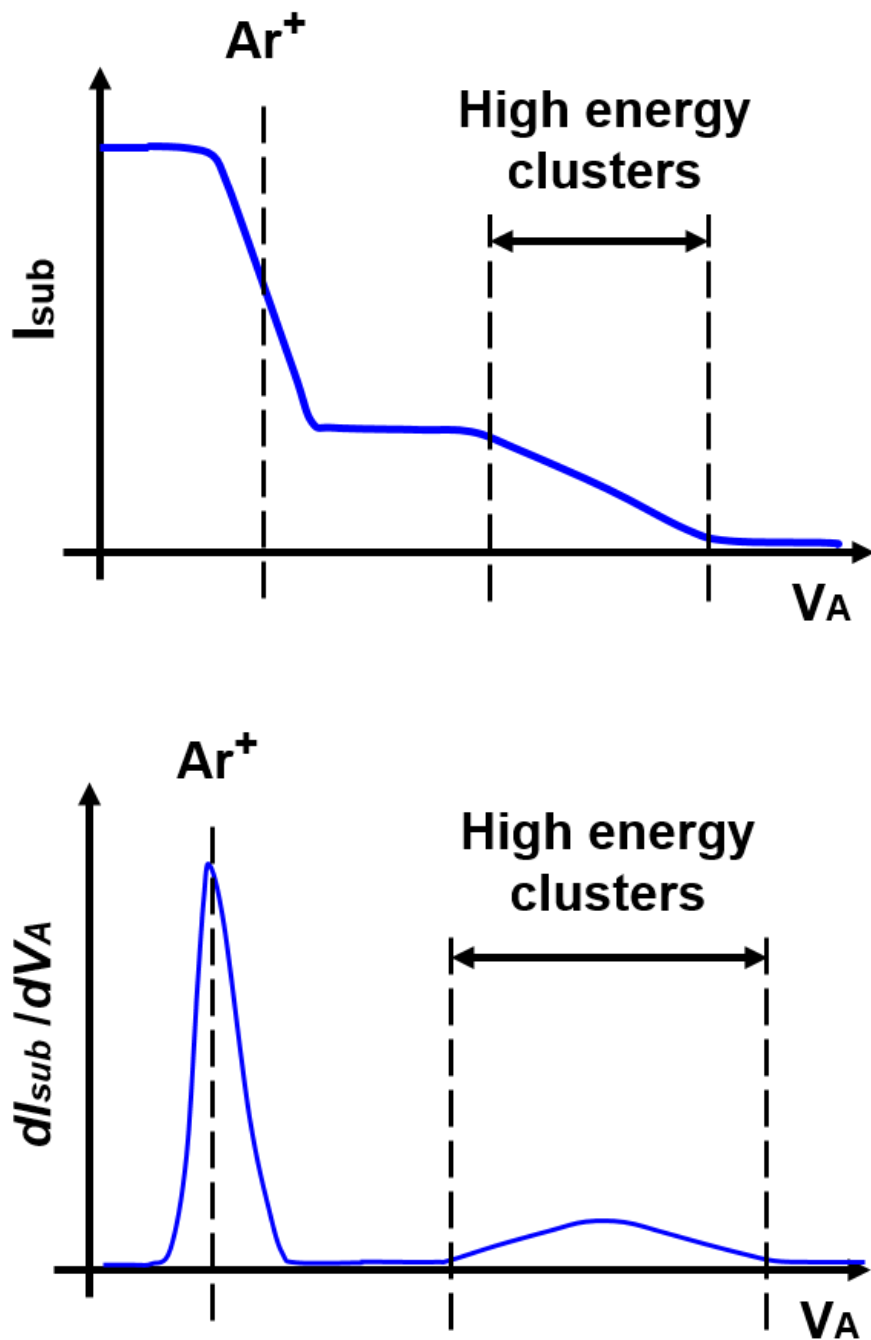
Figure 34. Schematics of estimation of I-V curve and energy distribution of high energy clusters.

Reference

[1] P. Hartman, Crystal Growth: An Introduction. 1973, Wiley, Amsterdam-London, 1974.

[2] W. R. Wilcox, L. L. Regel, Handbook of crystal growth. Vol. 1: Fundamentals. a: thermodynamics and kinetics; b: transport and stability edited by DTJ Hurle, Acta Crystallographica Section A: Foundations of Crystallography 50(5) (1994) 652-653.

[3] L. Boufendi, A. Plain, J. P. Blondeau, A. Bouchoule, C. Laure, M. Toogood, Measurements of particle size kinetics from nanometer to micrometer scale in a low-pressure argon-silane radio-frequency discharge, 60(2) (1992) 169-171.

[4] A. A. Howling, L. Sansonnens, J. -L. Dorier, C. Hollenstein, Negative hydrogenated silicon ion clusters as particle precursors in RF silane plasma deposition experiments, Journal of Physics D: Applied Physics 26(6) (1993) 1003.

[5] S. Veprek, O. Ambacher, W. Rieger, K. Schopper, M.G.J. Veprek-Heijman, Clusters in a silane glow discharge: Mechanism of their formation and how to avoid them, MRS Online Proceedings Library Archive 297 (1993) 13-18.

[6] A. Garscadden, B. Ganguly, P. Haaland, J. Williams, Overview of growth and behaviour of clusters and particles in

plasmas, 3(3) (1994) 239.

[7] E. Stoffels, W. W. Stoffels, G. M. W. Kroesen, F. J. De Hoog, Dust formation and charging in an Ar/SiH4 radio-frequency discharge, Journal of Vacuum Science Technology A: Vacuum, Surfaces, Films 14(2) (1996) 556−561.

[8] N. M. Hwang, D. Y. Yoon, Thermodynamic approach to the paradox of diamond formation with simultaneous graphite etching in the low pressure synthesis of diamond, Journal of crystal growth 160(1−2) (1996) 98−103.

[9] N. M. Hwang, J. H. Hahn, D. Y. Yoon, Charged cluster model in the low pressure synthesis of diamond, Journal of crystal growth 162(1−2) (1996) 55−68.

[10] N. M. Hwang, J. H. Hahn, D. Y. Yoon, Chemical potential of carbon in the low pressure synthesis of diamond, Journal of crystal growth 160(1−2) (1996) 87−97.

[11] N. −M. Hwang, D. −Y. Kim, Charged clusters in thin film growth, International materials reviews 49(3−4) (2004) 171−190.

[12] N. −M. Hwang, D. −K. Lee, Charged nanoparticles in thin film and nanostructure growth by chemical vapour deposition, Journal of Physics D: Applied Physics 43(48) (2010) 1−38.

[13] M. Niederberger, H. Cölfen, Oriented attachment and mesocrystals: non−classical crystallization mechanisms based

on nanoparticle assembly, Physical chemistry chemical physics 8(28) (2006) 3271−3287.

[14] J. −M. Huh, D. −Y. Yoon, D. −Y. Kim, N. −M. Hwang, Effect of substrate materials in the low−pressure synthesis of diamond: approach by theory of charged clusters, Zeitschrift für Metallkunde 96(3) (2005) 225−232.

[15] C. −S. Kim, Y. −B. Chung, W. −K. Youn, N. −M. Hwang, Generation of charged nanoparticles during the synthesis of carbon nanotubes by chemical vapor deposition, Carbon 47(10) (2009) 2511−2518.

[16] C. −S. Kim, Y. −B. Chung, W. −K. Youn, N. −M. Hwang, Generation of Charged Nanoparticles during Synthesis of ZnO Nanowires by Carbothermal Reduction, Aerosol Science and Technology 43(2) (2009) 120−125.

[17] C. −S. Kim, W. −K. Youn, N. −M. Hwang, Generation of charged nanoparticles and their deposition during the synthesis of silicon thin films by chemical vapor deposition, Journal of Applied Physics 108(1) (2010) 1−6.

[18] W. −K. Youn, S. −S. Lee, J. −Y. Lee, C. −S. Kim, N. −M. Hwang, S. Iijima, Comparison of the Deposition Behavior of Charged Silicon Nanoparticles between Floating and Grounded Substrates, The Journal of Physical Chemistry C 118(22) (2014) 11946−11953.

[19] R. S. Wagner, W .C. Ellis, Vapor-liquid-solid mechanism of single crystal growth, Applied physics letters 4(5) (1964) 89-90.

[20] R. Q. Zhang, Y. Lifshitz, S. T. Lee, Oxide-assisted growth of semiconducting nanowires, Advanced Materials 15(7-8) (2003) 635-640.

[21] N. P. Rao, S. Nijhawan, T. Kim, Z. Wu, S. Campbell, D. Kittelson, P. McMurry, C. C. Cheng, E. Mastromatteo, Investigation of Particle Generation during the Low-Pressure Chemical Vapor Deposition of Borophosphosilicate Glass Films, Journal of the Electrochemical Society 145(6) (1998) 2051-2057.

[22] K. Matsumoto, T. Horide, K. Osamura, M. Mukaida, Y. Yoshida, A. Ichinose, S. Horii, Enhancement of critical current density of YBCO films by introduction of artificial pinning centers due to the distributed nano-scaled Y_2O_3 islands on substrates, Physica C 412 (2004) 1267-1271.

[23] P. R. i Cabarrocas, Plasma enhanced chemical vapor deposition of amorphous, polymorphous and microcrystalline silicon films, Journal of non-crystalline solids 266 (2000) 31-37.

[24] P. R. i Cabarrocas, Plasma enhanced chemical vapor deposition of silicon thin films for large area electronics,

Current Opinion in Solid State Materials Science 6(5) (2002) 439-444.

[25] Z. Z. Fang, H. Wang, Densification and grain growth during sintering of nanosized particles, International Materials Reviews 53(6) (2008) 326-352.

[26] J. M. Yuk, J. Park, P. Ercius, K. Kim, D. J. Hellebusch, M. F. Crommie, J. Y. Lee, A. Zettl, A. P. Alivisatos, High-resolution EM of colloidal nanocrystal growth using graphene liquid cells, Science 336(6077) (2012) 61-64.

[27] B. W. Clare, G. Talukder, P. J. Jennings, J. C. L. Cornish, G. T. Hefter, Effect of charge on bond strength in hydrogenated amorphous silicon, Journal of computational chemistry 15(6) (1994) 644-652.

[28] C. T. T. GmbH, Low Pressure Chemical Vapor Deposition - Technology and Equipment. https://www.crystec.com/klllpcvde. htm.

[29] C. T. T. GmbH, Plasma Enhanced Chemical Vapor Deposition, PECVD. https://www.crystec.com/tridepe.htm.

[30] J. Tavares, E. J. Swanson, S. Coulombe, Plasma synthesis of coated metal nanoparticles with surface properties tailored for dispersion, Plasma Processes Polymers 5(8) (2008) 759-769.

[31] R. E. I. Schropp, B. Stannowski, A. M. Brockhoff, P. A. T.

T. Van Veenendaal, J. Rath, Hot wire CVD of heterogeneous and polycrystalline silicon semiconducting thin films for application in thin film transistors and solar cells, Materials Physics Mechanics 1 (2000) 73−82.

[32] K. K. S. Lau, J. A. Caulfield, K. K. Gleason, Structure and morphology of fluorocarbon films grown by hot filament chemical vapor deposition, Chemistry of Materials 12(10) (2000) 3032−3037.

[33] C. A. D. Dion, J. R. Tavares, Photo−initiated chemical vapor deposition as a scalable particle functionalization technology (a practical review), Powder technology 239 (2013) 484−491.

[34] G. Wahl, P. B. Davies, R. F. Bunshah, B. A. Joyce, C. D. Bain, G. Wegner, M. Remmers, K. Hieber, J.−E. Sundgren, P. K. Bachimann, S. Miyazawa, A. Thelen, H. Strathmann, Thin Films, Encyclopedia of industrial chemistry, Wiley−VCH Verlag GmbH & Co. KGaA, Weinheim, 2012, pp. 520−554.

[35] A. Asatekin, M.C. Barr, S. H. Baxamusa, K. K. S. Lau, W. Tenhaeff, J. Xu, K. K. Gleason, Designing polymer surfaces via vapor deposition, Materials Today 13(5) (2010) 26−33.

[36] I. Stassen, M. Styles, G. Grenci, H. Van Gorp, W. Vanderlinden, S. De Feyter, P. Falcaro, D. De Vos, P. Vereecken, R. Ameloot, Chemical vapour deposition of zeolitic imidazolate

framework thin films, Nature materials 15(3) (2016) 304.

[37] A. T. Servi, E. Guillen-Burrieza, D. M. Warsinger, W. Livernois, K. Notarangelo, J. Kharraz, H. A. Arafat, K. K. Gleason, The effects of iCVD film thickness and conformality on the permeability and wetting of MD membranes, Journal of Membrane Science 523 (2017) 470-479.

[38] N. Selvakumar, H. C. Barshilia, Review of physical vapor deposited (PVD) spectrally selective coatings for mid-and high-temperature solar thermal applications, Solar energy materials solar cells 98 (2012) 1-23.

[39] J. F. Hanlon, R. J. Kelsey, H. Forcinio, Handbook of package engineering, 3 ed., CRC press1998.

[40] E. Fortunato, P. Barquinha, R. Martins, Oxide semiconductor thin-film transistors: a review of recent advances, Advanced materials 24(22) (2012) 2945-2986.

[41] Wikipedia, Sputter deposition. https://en.wikipedia.org/wiki/Sputter_deposition.

[42] A. L. Gobbi, P. A. P. Nascente, D. C. Sputtering, in: Q. J. Wang, Y.-W. Chung (Eds.) Encyclopedia of Tribology, Springer Science+Business Media, New York, 2013.

[43] R. R. Boyer, An overview on the use of titanium in the aerospace industry, Materials Science and Engineering A213 (1996) 103-114.

[44] C. N. Elias, J. H. C. Lima, R. Valiev, M. A. Meyers, Biomedical Applications of Titanium and its Alloys, JOM (2008) 46-49.

[45] L. Huang, B. Liu, Q. Zhu, S. Chen, M. Gao, F. Qin, D. Wang, Low resistance Ti Ohmic contacts to 4H-SiC by reducing barrier heights without high temperature annealing, Applied Physics Letters 100(26) (2012) 1-4.

[46] M. Kaur, K. Singh, Review on titanium and titanium based alloys as biomaterials for orthopaedic applications, Materials Science & Engineering C 102 (2019) 844-862.

[47] M. Suzuki, T. Kawakami, T. Arai, S. Kobayashi, Y. Koide, T. Uemura, N. Shibata, M. Murakami, Low-resistance Ta/Ti Ohmic contacts for p-type GaN, Applied Physics Letters 74(2) (1999) 275-277.

[48] C. Ting, M. Wittmer, The use of titanium-based contact barrier layers in silicon technology, Thin Solid Films 96 (1982) 327-345.

[49] V. Chawla, R. Jayaganthan, A.K. Chawla, R. Chandra, Morphological study of magnetron sputtered Ti thin films on silicon substrate, Materials Chemistry and Physics 111(2-3) (2008) 414-418.

[50] V. Chawla, R. Jayaganthan, A. K. Chawla, R. Chandra, Microstructural characterizations of magnetron sputtered Ti

films on glass substrate, Journal of Materials Processing Technology 209(7) (2009) 3444-3451.

[51] A. Y. Chen, Y. Bu, Y. T. Tang, Y. Wang, F. Liu, X. F. Xie, J. F. Gu, Deposition-rate dependence of orientation growth and crystallization of Ti thin films prepared by magnetron sputtering, Thin Solid Films 574 (2015) 71-77.

[52] J. B. O. Gonzalo F. Iriarte, Jorgen Westlinder, Fredrik Engelmark, Ilia V. Katardjiev, Synthesis of C-Axis-Oriented AlN Thin Films on high-conducting layers_Al, Mo, Ti, TiN, and Ni, ieee transactions on ultrasonics, ferroelectrics, and frequency control 52(7) (2005) 1170-1174.

[53] Y. L. Jeyachandran, B. Karunagaran, S. K. Narayandass, D. Mangalaraj, The effect of thickness on the properties of titanium films deposited by dc magnetron sputtering, Materials Science and Engineering: A 458(1-2) (2007) 361-365.

[54] J. H. Kwon, D. Y. Kim, K. -S. Kim, N. -M. Hwang, Preparation of Highly (002) Oriented Ti Films on a Floating Si (100) Substrate by RF Magnetron Sputtering, Electronic Materials Letters (2019).

[55] N. Muslim, Y. W. Soon, C. M. Lim, Y. N. Voo, Influence of sputtering power on properties of titanium thin films deposited by RF magnetron sputtering, ARPN Journal of Engineering and Applied Sciences 10(16) (2015) 7148-7189.

[56] J. Aizenberg, P. V. Braun, P. Wiltzius, Patterned Colloidal Deposition Controlled by Electrostatic and Capillary Forces, PHYSICAL REVIEW LETTERS 84(13) (2000) 2997-3000.

[57] A. Demortiere, A. Snezhko, M. V. Sapozhnikov, N. Becker, T. Proslier, I. S. Aranson, Self-assembled tunable networks of sticky colloidal particles, Nat Commun 5(3117) (2014) 1-7.

[58] J. A. Ferrar, M. J. Solomon, Kinetics of colloidal deposition, assembly, and crystallization in steady electric fields, Soft Matter 11 (2015) 3599-3611.

[59] B. Sadri, D. Pernitsky, M. Sadrzadeh, Aggregation and deposition of colloidal particles: Effect of surface properties of collector beads, Colloids and Surfaces A: Physicochemical and Engineering Aspects 530 (2017) 46-52.

[60] Z. Wang, B. He, G. Xu, G. Wang, J. Wang, Y. Feng, D. Su, B. Chen, H. Li, Z. Wu, H. Zhang, L. Shao, H. Chen, Transformable masks for colloidal nanosynthesis, Nat Commun 9(563) (2018) 1-9.

[61] J. -S. Jung, N. -M. Hwang, Non-Classical Crystallization of Thin Films and Nanostructures in CVD Process, in: S. Neralla (Ed.), Chemical Vapor Deposition - Recent Advances and Applications in Optical, Solar Cells and Solid State Devices, InTech, Janeza Trdine 9, 51000 Rijeka, Croatia, 2016, pp. 23-67.

[62] S. -S. Lee, C. -S. Kim, N. -M. Hwang, Generation of Charged Nanoparticles During the Synthesis of GaN Nanostructures by Atmospheric-Pressure Chemical Vapor Deposition, Aerosol Science and Technology 46(10) (2012) 1100-1108.

[63] N. -M. Hwang, Non-classical crystallization of thin films and nanostructures in CVD and PVD processes, Springer2016.

[64] I. -D. Jeon, M. C. Barnes, D. -Y. Kim, N. -M. Hwang, Origin of positive charging of nanometer-sized clusters generated during thermal evaporation of copper, Journal of Crystal Growth 247 (2003) 623-630.

[65] J. -S. Jung, S .-H. Lee, D. -S. Kim, K. -S. Kim, S. -W. Park, N. -M. Hwang, Non-classical crystallization of silicon thin films during hot wire chemical vapor deposition, Journal of Crystal Growth 458 (2017) 8-15.

[66] D. -S. Kim, N. -M. Hwang, Synthesis of nanostructures using charged nanoparticles spontaneously generated in the gas phase during chemical vapor deposition, Journal of Physics D: Applied Physics 51(46) (2018) 1-23.

[67] J. -W. Park, K. -S. Kim, N. -M. Hwang, Gas phase generation of diamond nanoparticles in the hot filament chemical vapor deposition reactor, Carbon 106 (2016) 289-294.

[68] S. −H. Park, J. −W. Park, S. −M. Yang, K. −H. Kim, N. −M. Hwang, Effect of Electric Bias on the Deposition Behavior of ZnO Nanostructures in the Chemical Vapor Deposition Process, The Journal of Physical Chemistry C 119 (2015) 25047−25052.

[69] W. −K. Youn, C. −S. Kim, J. −Y. Lee, S. −S. Lee, N. −M. Hwang, Generation of Charged Nanoparticles and Their Deposition Behavior under Alternating Electric Bias during Chemical Vapor Deposition of Silicon, The Journal of Physical Chemistry C 116 (2012) 25157−25163.

[70] S. −W. Park, J. −S. Jung, K. −S. Kim, K. −H. Kim, N. −M. Hwang, Effect of Bias Applied to the Substrate on the Low Temperature Growth of Silicon Epitaxial Films during RF−PECVD, Crystal Growth & Design 18(10) (2018) 5816−5823.

[71] S. −W. Yoo, S. −J. You, J. −H. Kim, D. −J. Seong, B. −H. Seo, N. −M. Hwang, Effect of substrate bias on deposition behaviour of charged silicon nanoparticles in ICP−CVD process, Journal of Physics D: Applied Physics 50(3) (2017) 1−9.

[72] B. B. Sahu, W. Long, J. G. Han, Highly conductive flexible ultra thin ITO nanoclusters prepared by 3−D confined magnetron sputtering at a low temperature, Scripta Materialia 149 (2018) 98−102.

[73] K. Hayasaki, Y. Takamura, N. Yamaguchi, K. Terashima,

T. Yoshida, Scanning tunneling microscopy of epitaxial $YBa_2Cu_3O_{7-x}$ films prepared by thermal plasma flash evaporation method, Journal of Applied Physics 81(3) (1997) 1222−1226.

[74] V. A. Matveev, N. K. Pleshanov, A. P. Bulkin, V. G. Syromyatnikov, The study of the oxidation of thin Ti films by neutron reflectometry, Journal of Physics: Conference Series 340(1) (2012) 1−4.

[75] G.F. Iriarte, J. Bjurstrom, J. Westlinder, F. Engelmark, I.V. Katardjiev, Synthesis of C−Axis−Oriented AlN Thin Films on high−conducting layers_Al, Mo, Ti, TiN, and Ni, IEEE transactions on ultrasonics, ferroelectrics, and frequency control 52(7) (2005) 1170−1174.

[76] N. Jackson, R. O' Keeffe, F. Waldron, M. O' Neill, A. Mathewson, Influence of aluminum nitride crystal orientation on MEMS energy harvesting device performance, Journal of Micromechanics and Microengineering 23(7) (2013) 9.

[77] A. T. Tran, O. Wunnicke, G. Pandraud, M. D. Nguyen, H. Schellevis, P. M. Sarro, Slender piezoelectric cantilevers of high quality AlN layers sputtered on Ti thin film for MEMS actuators, Sensors and Actuators A: Physical 202 (2013) 118−123.

[78] J. Xiong, H.−s. Gu, K. Hu, M.−z. Hu, Influence of substrate

metals on the crystal growth of AlN films, International Journal of Minerals, Metallurgy, and Materials 17(1) (2010) 98−103.

[79] L. I. Maissel, P. M. Schaible, Thin Films Deposited by Bias Sputtering, Journal of Applied Physics 36(1) (1965) 237−242.

[80] F. A. Smidt, Use of ion beam assisted deposition to modify the microstructure and properties of thin films, International Materials Reviews 35 (1990) 61−128.

[81] L. Zhang, L. Q. Shi, Z. J. He, B. Zhang, Y.F. Lu, A. Liu, B.Y. Wang, Deposition of dense and smooth Ti films using ECR plasma−assisted magnetron sputtering, Surface and Coatings Technology 203(22) (2009) 3356−3360.

[82] A. W. Burton, K. Ong, T. Rea, I. Y. Chan, On the estimation of average crystallite size of zeolites from the Scherrer equation: A critical evaluation of its application to zeolites with one−dimensional pore systems, Microporous and Mesoporous Materials 117(1−2) (2009) 75−90.

[83] Y. Hoshi, E. Suzukia, H. Shimizu, Control of crystal orientation of Ti thin films by sputtering, Electrochimica Acta 44 (1999) 3945−3952.

[84] H. Kersten, D. Rohde, J. Berndt, H. Deutsch, R. Hippler, Investigations on the energy influx at plasma processes by means of a simple thermal probe, Thin Solid Films 377−378 (2000) 585−591.

[85] Hitachi. Science, 2018. https://www.azom.com/article. aspx?ArticleID=15632.

[86] 염근영, 플라즈마 식각기술, 서울 : 미래컴, 서울, 2006.

국 문 초 록

티타늄 (Ti) 타겟을 사용하는 RF 스퍼터링 내에서 하전 된 나노 입자 (NP)의 생성이 확인되었고, 이들이 박막의 질에 미치는 영향에 대해 연구하였다. 하전 된 Ti 나노입자를 −70V, 0V, +5V, +15V 및 +30V의 바이어스로 비정질 탄소 맴브레인을 이용하여 30초 동안 포집한 후, 투과 전자 현미경 (TEM) 을 이용하여 조사하였다. 그 결과 기판의 바이어스의 크기가 양의 값으로 증가함에 따라, 포집 된 Ti 나노입자의 수는 감소하였다. 이는 포집 된 Ti 나노입자가 양으로 하전되어 있으므로, 양의 바이어스 값을 갖는 기판으로부터 쿨롱 힘에 의해 반발이 일어나는 것이다. 또한 포집 된 Ti 입자들이 박막 증착 거동에 미치는 영향을 확인해보고자 하였다. 이를 위해, 포집 실험과 동일한 세팅에서 −70V, 0V 및 +30V의 바이어스로 실리콘 (Si) 기판 상에 30분 동안 증착한 후, TEM, 전계 방출 주사 전자 현미경 (FESEM) 및 X− 선 반사율 (XRR)에 의해 분석하였다. 박막의 물성을 비교해 본 결과, −70V에서 증착 된 필름은 가장 높은 성장률, 결정성 및 밀도 값을 갖는 반면, + 30V에서 증착 된 박막은 가장 낮은 성장률, 결정성 및 밀도 값을 가졌다. 이는 −70V의 경우, 양으로 하전 된 Ti 나노입자가 가속되어 기판에 끌어 당겨지고 + 30V의 경우 기판 상에 대부분 중성 Ti 입자 중, TEM으로 관찰하기 어려운 매우 작은 사이즈의 입자들 (나노입자

혹은 원자)에 의해 증착되었기 때문으로 생각된다. 이러한 결과로부터 스퍼터링 내에서 하전 된 나노입자의 제어를 통해, 상온에서 고품질 박막을 얻을 수 있음을 알 수 있다. 특히, 기존에 금속 박막을 증착 시 주로 사용하는 DC 스퍼터링이 아닌 RF 스퍼터링을 사용할 경우 이온화율이 더욱 높기 때문에, 하전 된 나노입자를 이용 및 제어하는 것이 더욱 유리할 것으로 생각된다. 따라서 금속 박막의 질을 한층 더 향상시킬 수 있는 가능성을 가지고 있다. 이를 반도체 회로의 금속 배선 공정에 적용한다면, 최근 문제가 되고 있는 금속 배선의 저항을 낮출 수 있을 것으로 예상된다.

또한, RF 스퍼터링을 내에서 Si (100) 기판 위에 (002) 방향으로 우선 성장 된 Ti 박막을 증착하였다. 이는 기판을 전기적으로 플로팅 시킴으로써 얻을 수 있었으며, Ti 박막을 플로팅 된 기판과 접지된 기판에 동시에 증착한 후, 그 차이를 비교하였다. 이 후, XRD, SEM 및 TEM을 이용하여 분석한 결과, 전기적으로 플로팅 된 기판위에서 접지 된 기판보다 (002) 방향으로 우선 성장 된 Ti 박막을 얻을 수 있었고, 특히 20 mTorr에서 이러한 경향이 가장 강하게 나타났다. 이처럼 플로팅 된 기판과 접지 된 기판 사이의 증착 거동 차이가 생기는 원인의 한 가지 가능성으로는, 기판으로 입사하는 입자의 에너지 차이가 박막의 미세구조에 영향을 줄 것이라고 예상하였다. 이를 확인하기 위해, 스퍼터링 공정 동안 K-형 열전대에 의해 기판 온도를 측정하고, 이로부터 기판으로의 입사에너지를 계산하였다.

그 결과, 플로팅 기판의 입사 에너지는 접지 된 기판의 입사 에너지보다 20% 낮았다. 기존에 연구된 문헌에 따르면, 스퍼터링을 이용하여 Ti 박막을 증착할 때, 기판으로 입사하는 입자의 에너지가 작은 경우 (002) 방향으로 성장하고 입사하는 에너지가 큰 경우 (100) 방향으로 성장하는 경향이 보고된 바 있다. 이 실험의 경우 플로팅 기판의 경우 접지 된 기판보다 기판으로 입사하는 입자의 에너지가 작으므로, (002) 방향으로 성장하기에 유리한 것으로 예상된다. 이와 같이 (002) 방향으로 우선 성장 된 Ti 박막은 압전 소자에서 AlN 박막 아래에 사용되는 금속 박막으로 사용하기에 적합하다.

한편, 플라즈마 공정 중에 in-situ 플라즈마 진단을 수행할 필요가 있다. 그 이유는 동일한 플라즈마 조건이 유지되어야만 일관되고 신뢰할 수 있는 실험 결과를 얻을 수 있기 때문이다. 그러나, 플라즈마 상태는 작은 변화에 민감하고 전체 프로세스 및 결과에 영향을 줄 수 있다. 또한, 다양한 플라즈마 진단 기술은 전자 및 이온 온도, 플라즈마 밀도와 같은 플라즈마 상태의 정보를 광범위하게 제공할 수 있다. 따라서 위의 실험 과정 동안, in-situ 플라즈마 진단을 사용하여 플라즈마에서 중성 및 양으로 하전 된 Ar 및 Ti 종을 특성화 하였다. 먼저, 여러 공정 압력에서의 Ti 및 Ar 종의 존재 및 비율을 광학 방출 분광법 (OES)에 의해 조사 하였다. 또한, 양으로 하전 된 종의 에너지 분포는 이온 에너지 분석기에 의해 추정되었다. 이 결과를 이용하여, 양으로 하전 된 Ti 나노입자의 에너지 분포를

실험적으로 확인하였다. 이와 같이 플라즈마 공정 과정 및 결과를 올바르게 이해하기 위해서는 in-situ 플라즈마 진단이 권장된다.